RICE UNIVERSITY

Illuminating Biomolecular Interactions with Localized Surface Plasmon Resonance
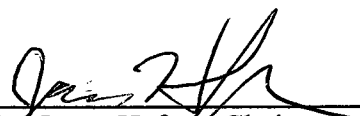
by

Kathryn M. Mayer

A THESIS SUBMITTED
IN PARTIAL FULFILLMENT OF THE
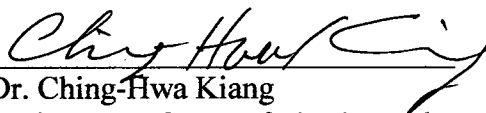REQUIREMENTS FOR THE DEGREE

Doctor of Philosophy

APPROVED, THESIS COMMITTEE:

Dr. Jason Hafner, Chair
Associate Professor of Physics
Associate Professor of Chemistry

Dr. Naomi Halas
Stanley C. Moore Professor of
      Electrical and Computer
      Engineering
Director, Laboratory for
      Nanophotonics
Professor of Bioengineering
Professor of Chemistry
Professor of Physics and Astronomy

Dr. Ching-Hwa Kiang
Assistant Professor of Physics and
      Astronomy
Assistant Professor of
      Bioengineering

HOUSTON, TX
APRIL 2010

UMI Number: 3421409

UMI®

Dissertation Publishing

ProQuest®

ABSTRACT

Illuminating Biomolecular Interactions with Localized Surface Plasmon Resonance

by

Kathryn M. Mayer

Noble metal nanoparticles exhibit localized surface plasmon resonance (LSPR), in which incident light causes a collective oscillation of a nanoparticle's free electrons. This phenomenon results in unique optical properties, including enhanced electric fields near the particle surface and an extinction peak at the resonant wavelength. The LSPR extinction peak's location is sensitive to the refractive index of the surrounding medium, especially in the volume closest to the particle surface. This makes plasmonic nanoparticles ideal for biosensing: their refractive index sensitivity can be used to transduce molecular binding signals. A method has been developed to use the optical extinction of films of gold nanorods to track antibody-antigen interactions in real time, resulting in a label-free kinetic immunoassay based on LSPR. Also, this method has been adapted to scattering spectra of single gold bipyramids. The single-particle approach has allowed the label-free detection of single biomolecules with kinetics information. These methods have future applications to both molecular biology and clinical assays.

ACKNOWLEDGEMENTS

First and foremost, I must thank my advisor, Prof. Jason Hafner. I count myself very lucky to have such a wonderful mentor, teacher, and supporter. He has dedicated a huge amount of time and energy over the past seven years to teaching me how to be a scientist, and working collaboratively with me. His encouragement and the great work environment he created got me through the pitfalls of grad school and enabled me to succeed. I also want to thank Prof. Naomi Halas for her mentoring and support, for providing me with so many opportunities throughout grad school, and for serving on my Ph.D. committee. I would like to thank Prof. Ching-Hwa Kiang for her support over the years, and for kindly serving on my Master's and Ph.D. committees. I must also thank Prof. Peter Nordlander for his guidance and help, and for his work in our collaboration on gold bipyramids.

Many thanks go to the wonderful chemist Seunghyun (Sean) Lee, with whom I have worked closely on the ensemble LSPR sensing experiments, and whose expertise in nanoparticle synthesis and surface chemistry has been invaluable. I also thank Dr. Feng Hao for his work on the FEM simulations of gold bipyramids. Thanks also to Prof. David Spivak of LSU for his work in our collaboration on the thrombin binding aptamer. I would like to thank Dr. Hongwei Liao, Dr. Colleen Nehl, and Amber Johnson, the original Hafner Lab students, who imparted so much knowledge to me as a beginning grad student. I must also thank Dr. Yi Yang and Dr. Nissanka Wickremasinghe, with whom I worked on membrane electrostatics before finding my way into plasmonics, and both of whom were wonderful to have as labmates! Thanks to my current labmates

TABLE OF CONTENTS

LIST OF TABLES

LIST OF FIGURES

LIST OF EQUATIONS

I.   Preface

From nuclear magnetic resonance to electron microscopy, x-ray diffraction to optical trapping, there is a long tradition of adapting physical science research methods to biological investigations. Over the past twenty years with the advent of nanomaterials and our increasing ability to design, manipulate, and study them, an array of new possibilities to interface with the biological realm has opened up. After all, biology happens at the nanoscale: a white blood cell is just ten microns wide, and the protein molecules that carry out its functions are truly nanoscale objects. We now have many nanoscale probes which can report local information from the vicinity of a single cell and even a single molecule. Here, we are interested in plasmonic nanoparticles which can focus light down to biomolecular dimensions.

Of course, developing plasmonic optical probes into useable research tools requires a full understanding of their physical properties and chemical manipulations, which is the subject of this thesis. Here I present the development of an immunoassay technique based on the physical phenomenon of localized surface plasmon resonance (LSPR) of gold nanoparticles. This work included the synthesis and surface modification of nanoparticles, the characterization of the structure and optical properties of the nanoparticles, the development of bioconjugation methods for the particles, the design of the immunoassay itself (using optical methods), and the kinetic and statistical analyses of both ensemble data and single-particle, single-molecule data. The results include the first demonstration of LSPR used to measure the kinetics of a biomolecular process. I also

report the first measurement of single molecule interactions by LSPR, and one of the only

label-free methods available for the study of single molecule interactions.

II. Introduction

Localized Surface Plasmon Resonance

A plasmon is a collective oscillation of the free electrons in a noble metal. It can be described as a quantum of plasma oscillation (thus the *–on* suffix); however, this terminology is somewhat misleading as the phenomenon itself is purely classical. One can think of these plasmon oscillations as mechanical oscillations of the electron gas of a metal, the presence of an external electric field causing displacements of the electron gas with respect to the fixed ionic cores. For bulk plasmons, these oscillations occur at the plasma frequency and have energy:

$$E_p = \hbar \sqrt{\frac{ne^2}{m\varepsilon_0}} \tag{1}$$

where *n* is the electron density, *e* is the electron charge, and *m* is the electron mass. (Here, bulk refers to materials with an extent large compared to the wavelength of light in all three dimensions.)

At the surface of a metal, plasmons take the form of surface plasmon polaritons (SPPs), also simply called surface plasmons (Fig. 1a). Surface plasmons can be excited optically or electronically, and can have standing and/or propagating SPP modes. Light can be coupled into surface plasmons through a grating or a defect in the metal surface. Because it is the oscillating electric field of the incoming plane wave that excites surface plasmons, light with a high angle of incidence (that is, with wave vector **k** nearly parallel to the surface) couples most efficiently.

a   b

-    +   -   +   -   +

↕
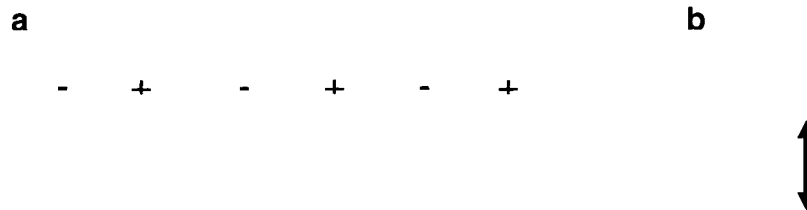
Figure 1. Illustrations of (**a**) a surface plasmon and (**b**) a localized surface plasmon.

When a surface plasmon is confined to a particle of a size comparable to the wavelength of light, *i.e.*, a nanoparticle, all of the particle's free electrons participate in the collective oscillation and it is termed a localized surface plasmon (LSP, Fig. 1b). The LSP has two important effects. First, electric fields near the particle's surface are greatly enhanced, this enhancement being greatest at the surface and falling off with distance. Second, the particle's optical extinction now has a maximum at the plasmon resonant frequency, which occurs at visible wavelengths for noble metal nanoparticles. This extinction peak depends on the refractive index of the surrounding medium, and is the basis for the sensing applications to be described. To understand in depth how this localized surface plasmon resonance (LSPR) arises, we must turn to scattering theory.

In the early 20th century, Gustav Mie developed an analytical solution to Maxwell's equations that describes the scattering and absorption of light by spherical particles[1]. (Mie's theory is more general than Rayleigh's, but it does reduce to Rayleigh scattering for very small particles.) Finding the scattered fields produced by a plane wave incident on a homogeneous conducting sphere results in the following scattering, extinction, and absorption cross sections[2]:

$$\sigma_{sca} = \frac{2\pi}{|k|^2} \sum_{L=1}^{\infty} (2L+1)\left(|a_L|^2 + |b_L|^2\right) \qquad (2)$$

$$\sigma_{ext} = \frac{2\pi}{|k|^2} \sum_{L=1}^{\infty} (2L+1)[\mathrm{Re}(a_L + b_L)] \tag{3}$$

$$\sigma_{abs} = \sigma_{ext} - \sigma_{sca} \tag{4}$$

Where k is the incoming wavevector and L are integers representing the dipole, quadrupole, etc., modes of the scattering. In the above expressions, a_L and b_L are the following functions, composed of the Riccati-Bessel functions ψ_L and χ_L:

$$a_L = \frac{m\psi_L(mx)\psi_L'(x) - \psi_L'(mx)\psi_L(x)}{m\psi_L(mx)\chi_L'(x) - \psi_L'(mx)\chi_L(x)} \tag{5}$$

$$b_L = \frac{\psi_L(mx)\psi_L'(x) - m\psi_L'(mx)\psi_L(x)}{\psi_L(mx)\chi_L'(x) - m\psi_L'(mx)\chi_L(x)} \tag{6}$$

Here, $m = n / n_m$ where n is the complex refractive index of the metal and n_m is the real refractive index of the surrounding medium. Also, $x = k_m r$, where r is the radius of the particle. (Note that $k_m = 2\pi/\lambda_m$ is defined as the wavenumber in the medium rather than the vacuum wavelength.) Figure 2 shows the Mie scattering cross section for metal spheres of varying sizes, showing the preponderance of forward scattering for particles having $x = 3$ or larger.[2]
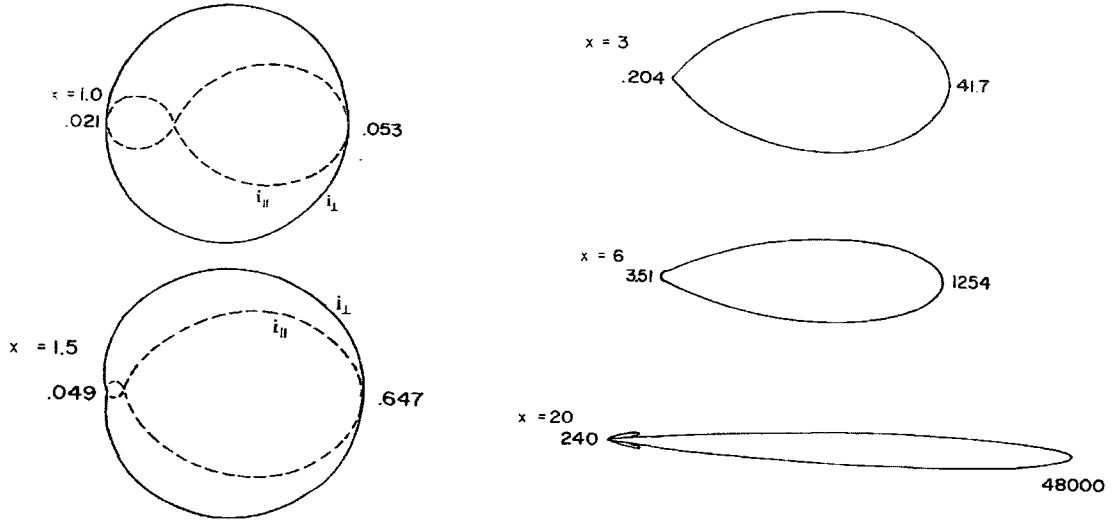
Figure 2. Mie scattering cross sections of metal spheres, taken from Bohren and Huffman. Light is incident from the left.

For small particles, it suffices to calculate only the $L = 1$ dipole term of the Mie theory expansion; this is called the dipole approximation. To gain an understanding of the resonance behavior and its dependence on the dielectric constant of the medium, we must make the dipole approximation, as well as the small-particle approximation; for x $<< 1$ the Riccati-Bessel functions simplify, yielding the frequency-dependent expression:

$$\sigma_{ext}(\omega) = \sigma_{abs}(\omega) = 9\frac{\omega}{c}\varepsilon_m^{3/2}V\frac{\varepsilon_2(\omega)}{[\varepsilon_1(\omega)+2\varepsilon_m]^2 + \varepsilon_2(\omega)^2} \tag{7}$$

Here, c is the speed of light, V is the particle volume, ε_m is the dielectric constant of the medium, ε_1 is the real part of the dielectric function of the metal, and ε_2 is the imaginary part of the dielectric function of the metal. Note that for small particles, the scattering is negligible, so we set $\sigma_{ext} = \sigma_{abs}$. In Figure 3, the complex dielectric functions of silver and gold are plotted, as experimentally determined by Johnson and Christy[3]. The absorption cross section will be maximized when the denominator in the above expression is minimized, a condition that will be met when $\varepsilon_1 = -2\varepsilon_m$. This explains the

dependence of the LSPR extinction peak on the surrounding dielectric environment. For example, for gold particles in water ($\varepsilon_m \approx 1.7$), the expected wavelength where $\varepsilon_1 = -2\ \varepsilon_m$ is about 520 nm, according to the real dielectric function for gold in Fig. 3a. And indeed, the experimentally observed absorption spectrum of gold colloid has a strong peak at that wavelength (Fig. 3c). As this example illustrates, the sensitivity to ε_m originates from the slope of the real part of the dielectric function in the observed wavelength range. Also note that for a given external dielectric constant, the LSPR wavelength for silver will be bluer (shorter) than that for gold. The imaginary part of the dielectric function also plays a role, relating to the damping, *i.e.*, resonance peak broadening, that is observed. Silver suffers lower losses than gold, as implied by Fig. 3b; however, gold is usually used in our experiments as it is easier to work with chemically and less prone to oxidation.
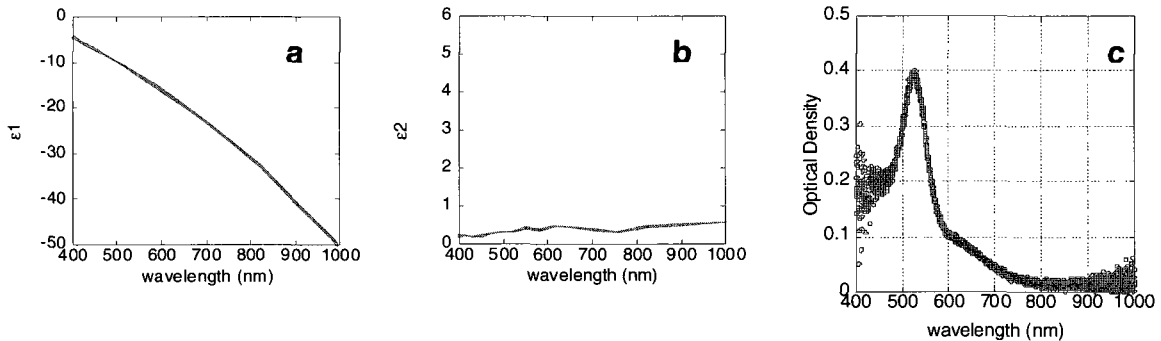
Figure 3. (a) Real and (b) imaginary parts of the complex dielectric functions of silver and gold. (c) Absorption spectrum of gold colloid solution.

Note that the optical extinction of gold colloid as shown in Figure 3c was unknowingly exploited for centuries before plasmon resonance was understood. Stained glass from the ancient world, such as the Lycurgus cup from second century Rome, owes its unusual optical properties to gold colloid embedded in the glass[4]. (See Figure 4.) When illuminated from the outside, the cup appears green due to light scattering at the

resonance wavelength, and when illuminated from the inside, it appears red due to the effect of resonant absorption on the transmitted light.   Michael Faraday first demonstrated this property of gold colloid in the 1850s, and his results inspired Mie's theoretical work that is described above.
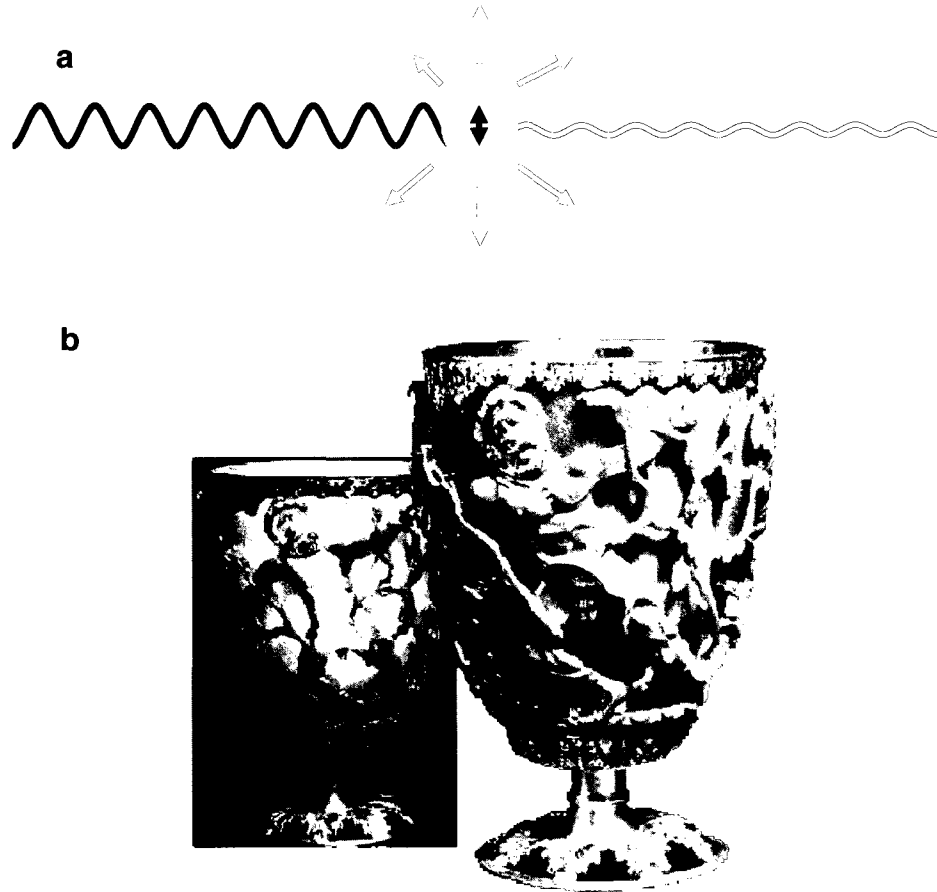
Figure 4. (a) Schematic of the LSPR extinction. (b) The Lycurgus cup, made from stained glass incorporating gold colloid.

To find the functional form of the LSPR peak wavelength's dependence on the dielectric function of the medium[5], one can use the analytical, frequency-dependent form for ε_1 from the Drude model of the electronic structure of metals:

$$\varepsilon_1 = 1 - \frac{\omega_p^{\,2}}{\omega^2 + \gamma^2} \qquad (8)$$

Where ω_p is the plasma frequency and γ is the damping parameter of the bulk metal. For the UV-visible region, $\gamma << \omega_p$ so the above can be simplified to:

$$\varepsilon_1 = 1 - \frac{\omega_p^{\,2}}{\omega^2} \qquad (9)$$

Using this expression for ε_1 and setting $\varepsilon_1 = -2\,\varepsilon_m$ (the resonance condition), one obtains the following:

$$\omega_{max} = \frac{\omega_p}{\sqrt{2\varepsilon_m + 1}} \qquad (10)$$

Where ω_{max} is the LSPR peak frequency. Converting from frequency to wavelength via $\lambda = 2\pi c\,/\,\omega$, and then from dielectric constant to index of refraction via $\varepsilon_m = n^2$, also assuming $2\,\varepsilon_m >> 1$, the above expression becomes:

$$\lambda_{max} = \lambda_p \sqrt{2\varepsilon_m + 1} = \lambda_p \sqrt{2 n_m^{\,2} + 1} \qquad (11)$$

Where λ_{max} is the LSPR peak wavelength and λ_p is the wavelength corresponding to the plasma frequency of the bulk metal. Thus, we see that the dependence of LSPR peak wavelength on the refractive index ought to be *approximately* linear at optical frequencies; this is borne out in experiments. Note that neither the LSPR peak frequency nor wavelength is *strictly* linear with refractive index; this will be discussed further below as it is a source of some contention in the field. In fact, *both* are approximately linear over small ranges of n.

Mie theory as formulated above is strictly applicable only to spherical particles. In 1912, Richard Gans generalized Mie's result to spheroidal particles of any aspect ratio in the small particle approximation[6]. He found that the absorption cross-section for a prolate spheroid, analogous to that in Eqn. 7 above for a sphere, is:

$$\sigma_{abs} = \frac{\omega}{3c}\varepsilon_m^{3/2}V\sum_j \frac{\left(1/P_j^2\right)\varepsilon_2}{\left\{\varepsilon_1 + \left[(1-P_j)/P_j\right]\varepsilon_m\right\}^2 + \varepsilon_2^2} \qquad (12)$$

Here, the sum over j considers the three dimensions of the particle. P_j includes P_A, P_B, and P_C, termed depolarization factors, for each axis of the particle, where $A > B = C$ for a prolate spheroid. The effect of these factors is to anisotropically alter the effects of ε_1 and ε_2. Explicitly, they are:

$$P_A = \frac{1-e^2}{e^2}\left[\frac{1}{2e}\ln\left(\frac{1+e}{1-e}\right) - 1\right] \qquad (13)$$

$$P_B = P_C = \frac{1-P_A}{2} \qquad (14)$$

Where e is the following factor, which includes the particle aspect ratio R:[7, 8]

$$e = \left[1 - \left(\frac{B}{A}\right)^2\right]^{1/2} = \left(1 - \frac{1}{R^2}\right)^{1/2} \qquad (15)$$

The extinction spectrum resulting from Eqn. 12 has two peaks, one corresponding to the transverse plasmon mode from the x and y contributions to the sum, and the other corresponding to the longitudinal plasmon mode from the z contribution. Eqn. 12 also provides an intuitive understanding of the effect of aspect ratio on the LSPR peak wavelength. The factor weighting ε_m, which is 2 for spherical particles (Eqn. 7), is [(1 − P_j) / P_j], a quantity that increases with aspect ratio and can be much greater than 2. This leads to a red-shift of the plasmon peak with increasing aspect ratio, as well as increased sensitivity to the dielectric constant of the surrounding medium. Beyond these estimates for spheroids, particle shape plays a significant role in determining the LSPR spectrum[9, 10], but one which cannot be found analytically as above, and must be studied numerically.

LSPR Sensing

The simplest sensing application of LSPR-active particles is to detect changes in the bulk refractive index. As described above, the LSPR peak shift is approximately linear with changes in refractive index of the surrounding medium. Therefore, the refractive index sensitivity of a particular particle type is usually reported in nanometers of peak shift per refractive index unit (nm/RIU). As discussed above, the refractive index sensitivity for spheroidal particles is determined by the choice of metal and the particle size and aspect ratio. The LSPR sensitivity of particles of other shapes cannot be described analytically, but it has been shown experimentally and in electrodynamic simulations that particle shape plays a large role in determining the sensitivity. Over the past decade, a myriad of new nanoparticle shapes with ever increasing refractive index sensitivities have been developed.

LSPR can be measured through several spectroscopic methods. Measurements can be carried out on single particles or ensembles, and the peak shift can be measured in the absorption, scattering, or total extinction spectra. For small particles that do not scatter strongly, ensemble extinction methods are best, whereas for larger particles that scatter brightly, single particle dark field scattering measurements are possible. Figure 5 shows example spectra of three types of LSPR-active nanoparticles, highlighting the differences in these two types of measurements. For the gold nanorods shown, only ensemble extinction measurements are possible because their scattering is very weak due to their small size. For gold nanostars, the extinction is largely due to scattering, but there is an important distinction between ensemble and single particle measurements. Individual

nanostars' spectra vary greatly depending on their exact structure, and so in the single-particle spectrum, separate peaks corresponding to the arms of the nanostar can be seen, whereas the ensemble extinction is simply a broad peak made up of many overlapping spectra[11, 12]. For gold bipyramids, the ensemble extinction has two peaks, one due to the bipyramids and one due to sphere impurities in the sample. When single-particle scattering spectra are taken, a single peak due to the bipyramid is seen.

Particle Type   Ensemble Extinction   Single Particle Scattering
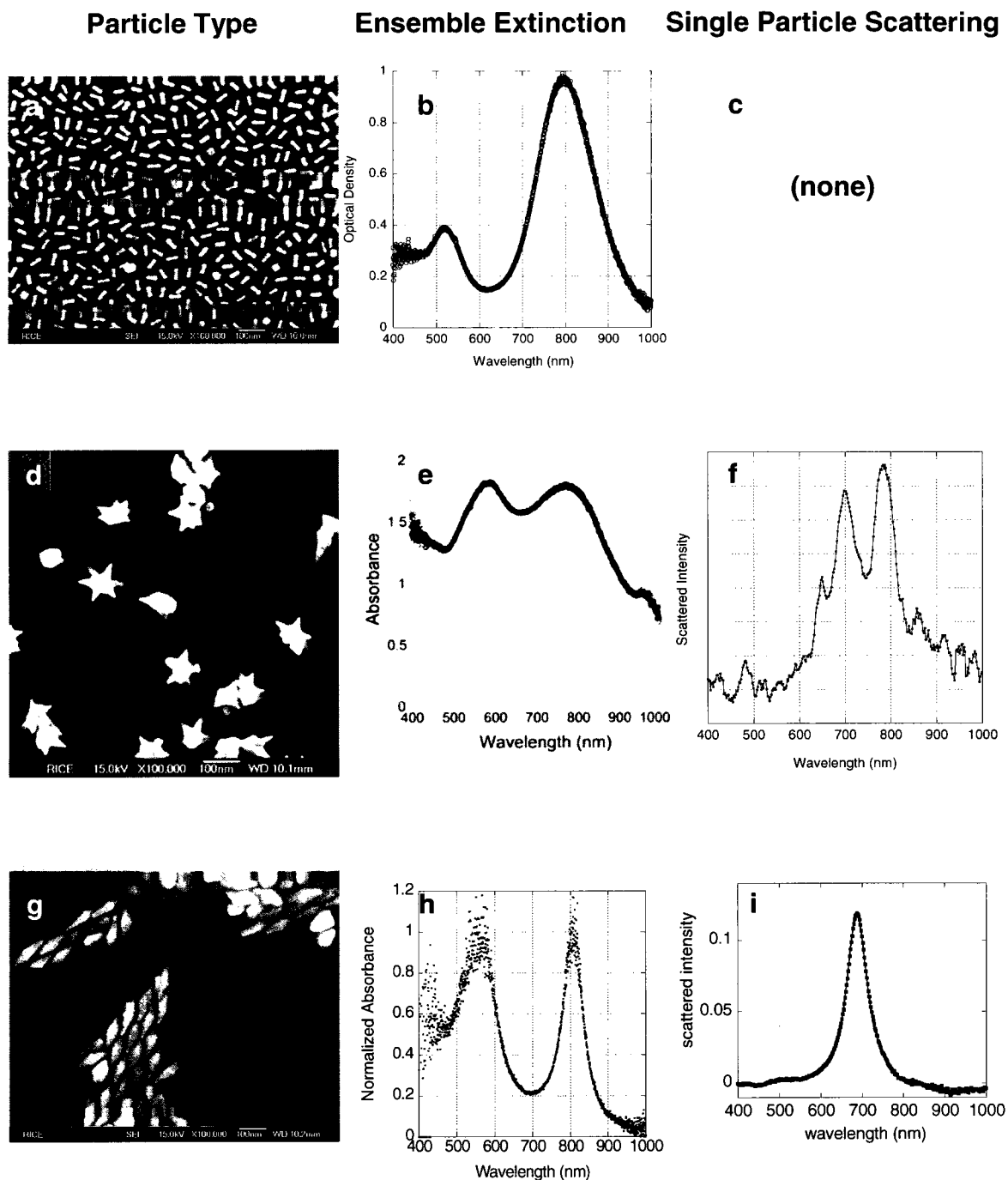
Figure 5. Comparison of the ensemble extinction and single particle scattering spectra for three particle types. (**a**) Gold nanorods. (**b**) Nanorod ensemble extinction. The two peaks are attributed to the transverse and longitudinal plasmon modes of the particle. (**c**) Nanorods scatter too weakly to obtain single particle scattering spectra. (**d**) Gold nanostars. (**e**) Nanostar ensemble extinction. Individual particle spectra are smeared out into a single broad peak in the near IR. (**f**) Nanostar single particle scattering spectrum. Multiple peaks in the near IR correspond to resonances of the arms of the star. (**g**) Gold bipyramids. (**h**) Bipyramid ensemble extinction. Two peaks are visible, attributable to bipyramids and spheres. (**i**) Bipyramid single particle scattering spectrum. A single bright, narrow peak is seen.

Table 1 summarizes some notable results on the LSPR sensitivities of various particle shapes from the past decade. In addition to the refractive index sensitivity, LSPR sensors are often characterized by a figure of merit (FOM) obtained by dividing the sensitivity by the resonance linewidth[13]; these values are given in the table as well. Because many in the field prefer to use energy units (eV) rather than wavelength (nm), all of the results are given in both units[14, 15]. There is some debate as to which units are more correct, but as the LSPR shift is not *strictly* linear with n in either nm or eV, the more important consideration is simply that the chosen units are used consistently across any comparison. One can see this from the second equality in Eqn. 11 for wavelength. For energy, one must convert to eV via:

$$E = \frac{hc}{\lambda} \qquad (16)$$

Rearranging Eqn. 11 then shows that E is also not linear with n:

$$E = \frac{hc}{\sqrt{2n_m^2 + 1}} \qquad (17)$$

Ref	Particle	Type	λ_{peak}		$\Delta\lambda$		shift/RIU		FOM
			nm	eV	nm	eV	nm	eV	
Tam 2004[16]	Au/SiO2 shell	ensemble	770	1.61	350	.732	314	.657	0.9
Sun 2002[17]	Au/AuS shell	ensemble	700	1.77	400	1.012	409	1.035	1.0
Wang 2006[18]	Au nanorice	ensemble	1600	.775	600	.291	801	.388	1.3
Underwood 1994[19]	Au sphere	ensemble	530	2.34	60	.265	090	.397	1.5
Raschke 2004[20]	Au/AuS shell	single	660	1.88	77	.220	117	.333	1.5
Sherry 2005[13]	Ag cube	single	510	2.43	91	.433	146	.695	1.6
Malinsky 2001[21]	Ag NSL	ensemble	564	2.20	104	.405	191	.745	1.8
Nehl 2006[11]	Au star	single	675	1.84	125	.340	238	.649	1.9
Lee 2009[22]	Au pyramid	single	680	1.82	114	.310	221	.450	2.2
Mock 2003[23]	Ag sphere	single	520	2.38	73	.335	160	.734	2.2
Bukasov 2007[24]	Au crescent	ensemble	1795	0.69	209	.08	596	.19	2.4
Mock 2003[23]	Ag triangle	single	760	1.63	80	.172	350	.751	4.4
Sherry 2005[13]	Ag cube-sub	single	430	2.88	22	.146	118	.792	5.4
Nehl 2006[11]	Au star	single	770	1.61	124	.260	665	1.410	5.4

Table 1. Summary of nanoparticle shapes and their refractive index sensitivities.

Of course, LSPR sensors can do much more than measure changes in bulk refractive index. As mentioned above, the field enhancement caused by the LSPR is strongest near the surface of the nanoparticle; therefore, only the nanoscale region around the particle is probed. This extremely localized sensing volume is a unique feature of plasmonic nanoparticles, and makes it possible to measure the local refractive index changes due to molecular binding at the particle surface through LSPR shifts. This is the basis of LSPR biosensing.

The simplest form of LSPR molecular sensing is to monitor a molecular layer binding directly to the gold surface of the nanoparticle. This has been shown to great effect with self-assembled monolayers (SAMs). SAMs are alkane carbon chains, which can be modified with a functional group at either end, that form tightly packed monolayers on a surface. Van Duyne and co-workers have measured the LSPR shift upon monolayer formation on silver nanoparticles[25, 26]. By using SAMs with different carbon chain lengths, they were able to discriminate changes of only a few angstroms of additional coating on the particle. In addition, they were able to describe how the LSPR sensitivity falls off with distance from the surface using SAMs of increasing length.

To demonstrate biomolecular sensing, most groups have investigated either biotin-streptavidin or antibody-antigen interactions. The protein streptavidin has an extremely high binding affinity for the vitamin biotin, and the pair is often used in biochemical applications as linker molecules; in LSPR sensing reports they are useful as a proof-of-concept for analyte detection. A more relevant system for biosensing demonstrations is an antibody and its specific antigen. Antibodies have an enormous capability to specifically bind an antigen molecule and are the basis for immunoassays, an important biomedical detection technology. Therefore, it is also important to demonstrate immunospecificity as a demonstration of clinical applicability. (See Chapter III for a further discussion of these previous reports of LSPR biosensing, with references.) An important consideration in all LSPR biosensors is the conjugation strategy for binding the capture molecule to the nanoparticles in a manner that will hold it near the nanoparticle, yet retain its biological function.

Another scheme for plasmonic biosensing relies on the large spectral shift that occurs when particles aggregate. Such experiments are carried out with particles suspended in solution and have been used for specific nucleotide sequence detection[27] and studying the melting behavior of DNA[28]. Note that these experiments are not truly label-free (a concept that will be discussed further below), as the nanoparticles themselves are serving as labels and the detected molecules are directly bound to nanoparticle surfaces.

In most cases, aggregation is to be avoided, as it is difficult to control. In some early solution-phase LSPR sensing experiments, in which the nanoparticles were coated with a capture antibody and the target was free, the likelihood of aggregation was reduced by using target antibodies with only one binding site (*i.e.*, monoclonal antibodies which bind only a single epitope on the target)[29]. A more common strategy against aggregation is to use particles fixed to a glass substrate. These particle-coated substrates can be made by top-down fabrication (lithography), bottom-up (self) assembly[30], or a technique that combines the two approaches (such as nanosphere lithography)[31]. An example of LSPR substrates fabricated by nanosphere lithography can be seen in Figure 6.
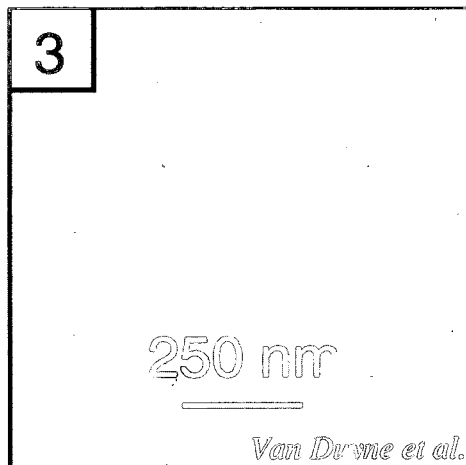
Figure 6. Silver nanotriangles for LSPR sensing, fabricated by nanosphere lithography, a technique in which films of dielectric nanospheres are assembled and silver is thermally evaporated on top. When the spheres are stripped away, Ag nanotriangles remain. (Image from Haes and Van Duyne[32].)

Immunoassay Basics

Antibodies are protein molecules that form the basis of the human immune system. They can to recognize and bind a specific molecular targets in a massive excess of non-specific targets through what can be thought of as a lock-and-key interaction between the antibody and target structures. The most common class of antibody, Immunoglobulin G (IgG), has a Y-shaped structure made up of two heavy chains and two light chains of amino acids (Fig. 7). The antibody is divided into three domains, the central F_c domain, and the branching F_a and F_b domains, which are the active sites of target (antigen) binding.
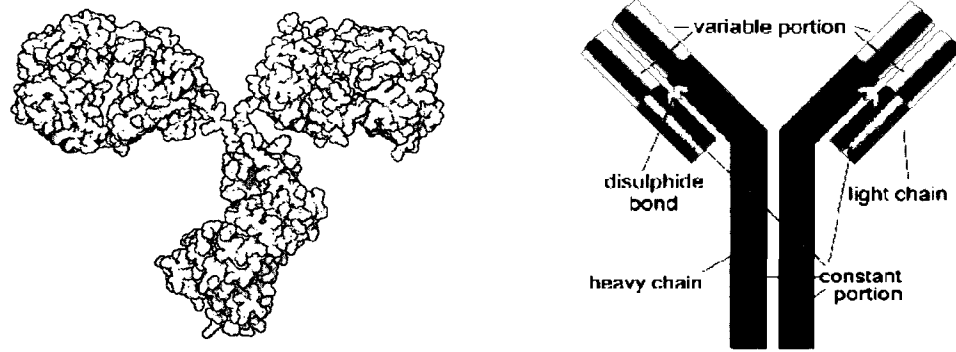
Figure 7. Structure and schematic of IgG.

In an immunoassay, the antibodies can be anchored to a substrate via the F_c domain, leaving the F_{ab} domains available for target binding and specific detection. In a label-free assay, the presence of the target itself provides the signal and no subsequent steps are needed. However, in most common immunoassays such as ELISA, a more complicated "sandwich" strategy is used, in which a different antibody is added after the target[33]. In many cases, a secondary antibody which recognizes one of the primary antibodies to the target is used in a final step; this secondary antibody is usually modified with a dye or other signaler. (See Fig. 8 for a schematic of traditional and label-free immunoassays, and see next section for a full explanation of ELISA.)

a   b

Enzyme-linked
secondary antibody

Primary antibody #2

Target

← Primary antibody #1
(capture antibody)
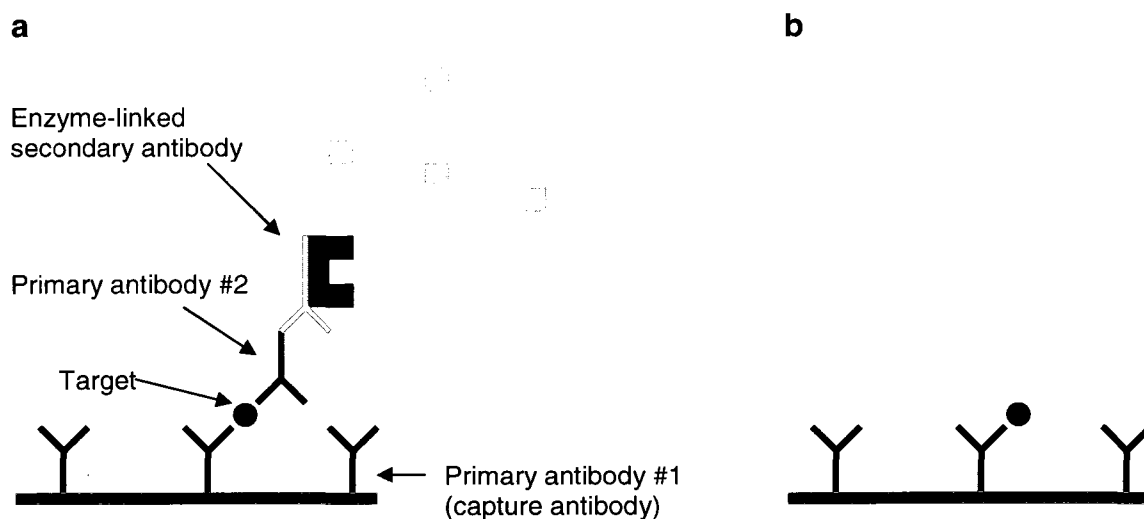
Figure 8. Schematics of (a) a traditional immunoassay (ELISA) and (b) a label-free immunoassay.

The most important measures of the quality of an immunoassay are the sensitivity and specificity. Sensitivity is self-explanatory; it simply refers to the lowest concentration of the target molecule that can be measured (also called the limit of detection). Specificity refers to the ability of an assay to distinguish between the target molecule and a nonspecifically bound unknown molecule; in other words, the avoidance of false positives. Although ELISAs are complicated, the steps as shown in Figure 8 enhance the sensitivity through amplification, and the specificity through multiple antibody interactions.

Label-Free Sensors

As mentioned above, most existing immunoassays rely on labeling the target molecule in some way. Depending on the technique, these labels can be radioisotopes, fluorophores, or enzymes. The most common immunoassay today, enzyme-linked

immunosorbant assay (ELISA), relies on an enzyme that activates a dye molecule only when bound to the target. These labeling strategies allow biologists to measure signals from miniscule amounts of sample due to their great amplification, *e.g.*, thousands of dye molecules activated for each target protein. However, attaching a label can remove a molecule from its native state, so for detailed studies of biomolecules in their natural state (or as close as possible), label-free techniques are needed.

A related technique to LSPR sensing, which actually predates it, is surface plasmon resonance (SPR) sensing. SPR utilizes the sensitivity of surface plasmon polaritons in a gold film to changes in refractive index, measured as the change in reflection angle of light passed through a prism and reflected off of the back of the film, as material binds to the other side of the film[34]. In practice, the difference in intensity between two fixed angles is often measured. (See Fig. 9.) SPR is a powerful surface analytical technique since it can detect submonolayer quantities of analyte at the gold film surface. In addition, in an immunoassay, these sensors can measure antigen concentrations as low as 1 nM, although they are still not as sensitive as ELISAs, which can detect concentrations as low as 0.5 ng/mL, or approximately 1 pM for a typical protein target. In addition to being label-free, the other great advantage of SPR sensors is that, through continuous optical measurements during the target exposure, they provide kinetics data. This allows the determination of binding constants from measurements at a single concentration, and is useful in studying the details of biomolecular interactions. One drawback is that SPR sensors lack a localized sensing volume, in many cases necessitating a thick polymer layer to cover the gold film surface that must be suffused with the capture antibody in order to generate enough binding signal to detect.
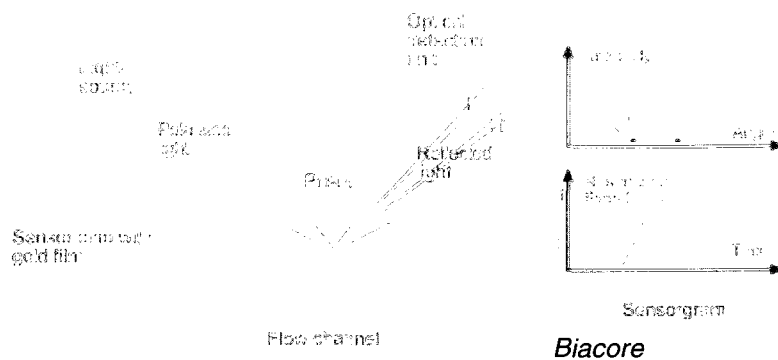
Figure 9. Schematic of a surface plasmon resonance (SPR) sensor.

Another type of label-free biosensor relies on force transduction. For example, one can measure the bending of a cantilever due to added mass and altered surface tension upon target binding. This technique has recently been used to investigate mechanisms of antibiotic resistance in bacteria by measuring the affinity of vancomycin (an antibiotic) for an array of target mucopeptides (molecules found on bacterial cell walls) in a multiplexed experiment. Vancomycin concentrations as low as 10 nM were used[35]. (See Figure 10.)
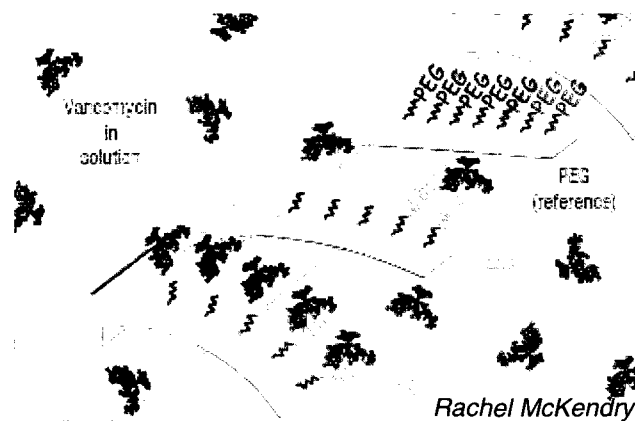
Figure 10. Label-free biosensing based on force sensors.

Label-free biosensing has also been achieved electronically in semiconductor nanowire systems that rely on measuring the change in current through the nanowire upon target binding. This technique has recently been used for ultrasensitive detection of the human blood protein cardiac troponin-T (cTnT), an important biomarker of myocardial infarction (heart attack). In that study, cTnT was measured at concentrations as low as 1 fg/mL (3 aM)[36]. (See Figure 11.)
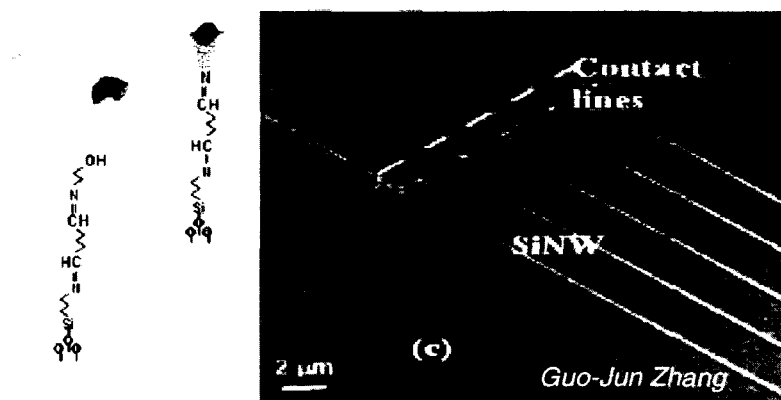
Figure 11. Label-free biosensing based on semiconductor nanowires.

However, optical methods like SPR, and now LSPR, are the most commonly used label-free methods.

Kinetics of Antibody-Antigen Interactions

To describe the interactions between antibodies fixed on a surface with a target protein in solution (as in LSPR sensors), a simple first-order binding kinetics model can be used. (This model is general for any surface binding reaction with a one-to-one binding ratio.) Here I will derive expressions for the rate constants of association and dissociation as well as the equilibrium constant for this interaction.

For an antibody-antigen pair C (for "capture") and T (for "target"), where CT is the complex formed by the two, we may write:

$$C + T \xleftrightarrow{k_{on}, k_{off}} CT \qquad (18)$$
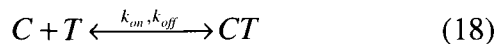
As in an immunoassay, let us assume that C is fixed on a surface with surface density $[C]$ and T is free in solution with volume concentration $[T]$. Complexes formed on the surface have density $[CT]$. Assuming one-to-one binding and a non-diffusion-limited first-order kinetic process, the change in the concentration of complexes over time is given by the differential equation:

$$\frac{\partial [CT]}{\partial t} = k_{on}[C][T] - k_{off}[CT] \qquad (19)$$

Where k_{on} and k_{off} are the association and dissociation rates of T. At equilibrium, the concentration of complexes is constant, and we define K_{eq} as the ratio of k_{on} and k_{off}.

$$K_{eq} = \frac{k_{on}}{k_{off}} = \frac{[CT]_{eq}}{[C]_{eq}[T]_{eq}} \qquad (20)$$

In a standard immunoassay, the substrate coated with C is exposed to T, where T is greatly in excess. At this time, an association curve is observed (see schematic in Fig. 12). Then, the substrate is rinsed, reducing $[T]$ in the solution to zero and resulting in the dissociation curve as T unbinds from C. Let us first examine the dissociation process.
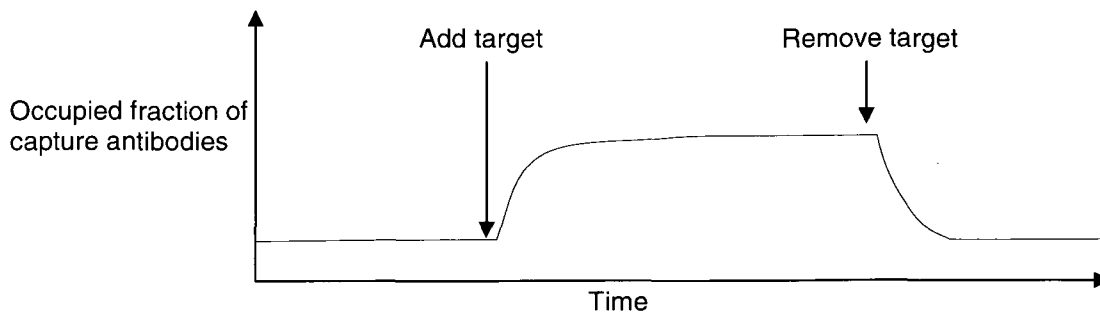
Figure 12. Schematic of antibody-antigen association and dissociation kinetics.

During dissociation, since $[T] = 0$, Eqn. 19 becomes the much simpler differential equation:

$$\frac{\partial [CT]}{\partial t} = -k_{off}[CT] \qquad (21)$$

The solution of which is a simple exponential decay function with decay constant k_{off}:

$$[CT] = Ae^{-k_{off}t} + B \qquad (22)$$

Where A and B are arbitrary constants. For the association process, the full Eqn. 19 must be used, but k_{off} is now a known constant, and one can replace $[C]$ with its initial value minus the amount of complexes formed (because C is fixed on the substrate):

$$\frac{\partial [CT]}{\partial t} = k_{on}[T]([C]_o - [CT]) - k_{off}[CT] \qquad (23)$$

Because the number of molecules of T forming complexes is negligible compared to the number in solution, one can also set $[T]$ to its constant initial value. Doing this, and rearranging, yields:

$$\frac{\partial [CT]}{\partial t} = k_{on}[C]_o[T]_o - (k_{off} + k_{on}[T]_o)[CT] \qquad (24)$$

This differential equation is soluble, and the solution is:

$$[CT] = \frac{k_{on}[C]_o[T]_o}{\left(k_{off} + k_{on}[T]_o\right)}\left[1 - e^{-\left(k_{off} + k_{on}[T]_o\right)t}\right] \qquad (25)$$

Because $[C]_0$ is unknown, the prefactor cannot be determined explicitly. However, one can fit experimental data with an arbitrary prefactor A and decay constant k_s.

$$[CT] = A\left[1 - e^{-k_s t}\right] \qquad (26)$$

Where $k_s = k_{off} + k_{on}[T]_0$. Since k_{off} and $[T]_0$ are known, once k_s is determined from a fit, one can then solve for k_{on}. Note that the prefactor in Eqn. 25 can be arranged into the form:

$$\frac{[CT]}{[C]_o} = \frac{\dfrac{k_{on}}{k_{off}}[T]_o}{\left(1 + \dfrac{k_{on}}{k_{off}}[T]_o\right)} \qquad (27)$$

This is analogous to the Langmuir isotherm for the adsorption of gas molecules to a surface:

$$\theta = \frac{KP}{1 + KP} \qquad (28)$$

Where θ is the absorption fraction, analogous to the fraction of capture antibodies occupied by a target; K is the association constant, analogous to $K_{eq} = k_{on}/k_{off}$; and P is the gas pressure, analogous to the target concentration.

III. A Label-Free Immunoassay Based Upon LSPR of Gold Nanorods

Background

Due to its label free nature and ability to provide kinetics data, SPR has become widely used in the study of biomolecular interactions, as well as in antibody screening for diagnostic and therapeutic applications[37, 38]. However, despite its analytical capabilities, SPR is not widely used in clinical immunoassays or other non-research applications owing to the complexity of the optical instrumentation and the need for precise temperature control. It has been suggested that LSPR sensing with nanoparticle substrates will preserve the virtues of SPR but greatly broaden the scientific and technological applications, since LSPR sensing is based on a simple optical extinction measurement, is not temperature sensitive, and requires only common laboratory equipment[32]. Furthermore, nanoparticles have a highly localized LSPR sensing volume which eliminates the need to trap the interacting molecules of interest in a polymer matrix to enhance the signal, as is often done in SPR measurements. As mentioned in the introduction, LSPR sensors based on nanoparticles affixed to a substrate, such as gold colloid films[30], or arrays of silver nanotriangles formed by nanosphere lithography[31], have met with much initial success. Further reports[39-58] include demonstrations of multiplexing[49, 59], the detection of medically relevant analytes in clinical samples[60, 61], and fiber-based sensors[39, 42]. Despite these successes, LSPR sensing is still not nearly as prevalent as SPR. For a summarized comparison of SPR and LSPR, see Figure 13 and Table 2.
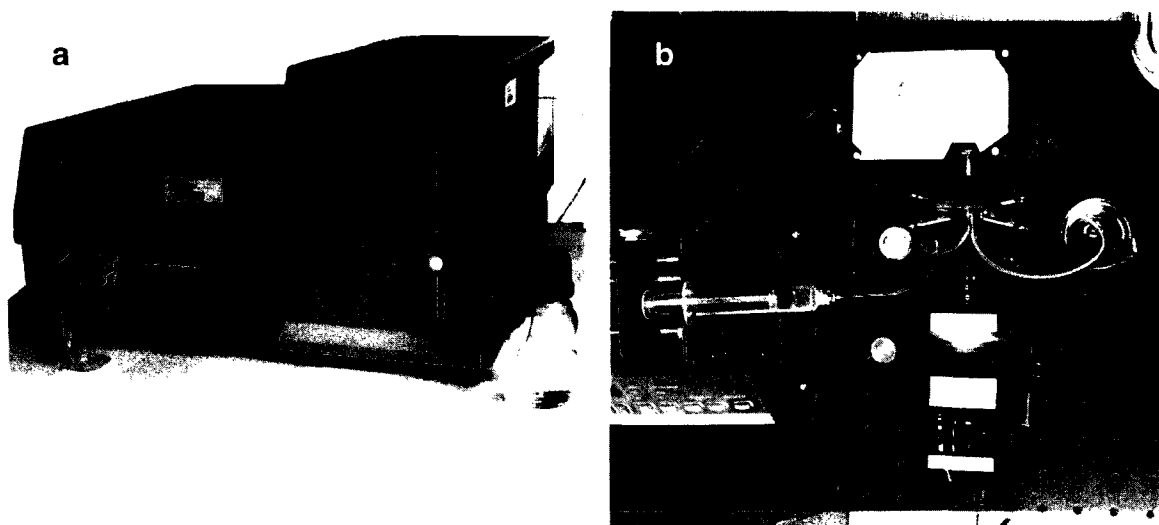
Figure 13. SPR vs. LSPR sensing. (a) Commercially available Biacore SPR instrument. (b) Simplest possible benchtop LSPR system.

	LSPR	SPR
Bulk dielectric sensitivity (nm/RIU)	10^2	10^6
Sensing distance (nm)	10	1000
Temperature sensitive?	No	Yes
Simple instrumentation?	Yes	No

Table 2. Overall comparison of LSPR and SPR sensors.

Thus far, biomolecular LSPR sensing studies have focused on biotin-streptavidin and antibody-antigen interactions, with a few exceptions[43, 45, 51, 62]. All reports find a red shift as the target binds to the nanoparticles, but most do not observe the correct equilibrium binding constant (K_{eq}) when the interaction is studied in detail. A few reports have measured the correct K_{eq} value for antibody-antigen interactions[41, 49], but these were from endpoint assays carried out at a series of concentrations as a titration or dose-response

experiment, rather than from kinetics. Therefore, the goal of this project was the real-time

analysis of antibody–antigen interactions by LSPR sensing. The system chosen was self-

assembled gold nanorod substrates (Figure 14)[63]. LSPR sensors have also been

fabricated by top-down methods, but using chemically synthesized particles and self-

assembled films allows us to fabricate a large number of substrates inexpensively, and

provides a more than adequate LSPR signal for sensing. Through careful control of the

substrate surface chemistry, we demonstrated the first successful measurement of the

kinetics of molecular binding by LSPR sensing.
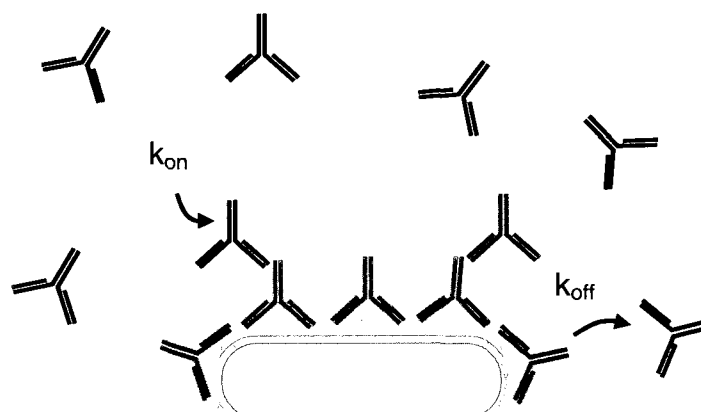
Figure 14. Schematic of the nanorod-based immunoassay. The nanorods are fixed to a
glass surface *via* an APTES monolayer, and then coated with a self-assembled
monolayer to which the capture antibody is coupled by carbodiimide cross-linking. The
substrate is exposed to antigen (in this case secondary antibodies) and the binding is
monitored *via* real-time absorption spectra.

Methods

Gold Nanorod Synthesis. Gold nanorods were prepared by surfactant-directed

chemical synthesis[63, 64]. All solutions were prepared fresh for each synthesis, except for

the hydrogen tetrachloroaurate(III) (Sigma, no. 520918), which was prepared as a 28 mM

stock solution from a dry ampoule and stored in the dark. An aliquot of the stock solution was diluted to 10 mM immediately before use. Gold seed particles were prepared by adding 250 μL of 10 mM hydrogen tetrachloroaurate(III) to 7.5 mL of 100 mM cetyltrimethylammonium bromide (CTAB) (Sigma, #H9151) in a plastic tube with brief, gentle mixing by inversion. Next, 600 μL of 10 mM sodium borohydride (Acros, #18930) was prepared from DI water chilled to 2–8 °C in a refrigerator and added to the seed solution *immediately* after preparation, followed by mixing by inversion for 1–2 min. The pale brown seed solution was stable and usable for several hours. The nanorod growth solution was prepared by adding the following reagents to a plastic tube in the following order and then gently mixing each by inversion: 425 mL of 100 mM CTAB, 18 mL of 10mM hydrogen tetrachloroaurate(III), and 2.7 mL of 10 mM silver nitrate (Acros, #19768). Next, 2.9 mL of 100 mM ascorbic acid (Fisher, #A61) was added and mixed by inversion, which changed the solution from brownish-yellow to colorless. To initiate nanorod growth, 1.8 mL of seed solution was added to the growth solution, mixed gently by inversion, and left still for three hours. During this time, the color changed gradually to dark purple, with most of the color change occurring in the first hour.

Gold Nanorod PEGylation. To stabilize the nanorods in a CTAB-free solution, they were coated with polyethylene glycol (PEG), a biocompatible polymer, according to the following procedure. One mL of CTAB-stabilized gold nanorods was centrifuged at 7000*g* to pellet the nanorods. The CTAB solution was decanted, and the pellet was resuspended in 2 mM potassium carbonate. This procedure leaves sufficient CTAB in the solution that the nanorods are stable for several hours. Twenty μL of 1 mM thiol

terminated methoxypoly(ethylene glycol) (mPEG-SH, 5000 MW, Nektar Theraputics) was added to the solution and left overnight to displace the CTAB[63]. The nanorods were then taken through at least two more centrifuge/decant cycles, resuspending each time in deionized water, to further reduce the CTAB concentration.

Gold Nanorod Substrate Fabrication. Glass microscopic slides (75 mm x 25 mm) were cleaned in piranha solution (3:1 H2SO4 : 30% H2O2), thoroughly rinsed with deionized water, and dried. (*WARNING: Piranha solution is very corrosive and must be handled with extreme caution; it reacts violently with organic materials.*) They were then immersed in an ethanolic solution of 5 mM aminopropyltriethoxysilane (APTES) (Sigma, #440140) overnight, rinsed with water, and dried. The APTES coated slides were then immersed in a PEGylated nanorod solution overnight. Once rinsed and dried, a uniform layer of gold nanorods remained on the surface with an absorbance of approximately 0.1 at the LSPR peak wavelength. To remove the mPEG-SH and other contaminants, the substrates were processed in an oxygen plasma cleaner at low power for 30 s in 200 mT oxygen (model PDC-32G, Harrick Scientific) and immersed in an ethanolic solution of 50 μM mercaptohexadecanoic acid (Sigma, #448303) and 50 μM mercaptoundecanol (Sigma, #447528) for 2.5 hours to form a mixed self-assembled monolayer (SAM).

The plasma cleaning step has no significant effect on the nanorod structure as observed by atomic force microscopy and scanning electron microscopy. Plasma cleaning does cause a small LSPR blue shift consistent with the removal of a thin polymer coating. In a variation of this procedure, nanorod films can also be fabricated on

the inside walls of a glass or quartz cuvette, to allow LSPR experiments to be carried out in an all-in-one spectrometer with a standard cuvette holder ("SPR in a cuvette").

Substrate Characterization. Substrates were characterized by scanning electron microscopy (SEM). To obtain detailed images of particle structure, substrates were fabricated as above, except on 1 cm x 1 cm silicon wafers rather than on glass, and the samples were imaged in high-vacuum mode in a JEOL 6500 SEM. To image the non-conductive glass substrates used in optical measurements, wet-mode environmental SEM (ESEM, FEI Quanta 400) was employed. In ESEM, the resolution is not as great as in traditional high-vacuum SEM, but it is possible to measure non-conductive samples in a water vapor environment. The water vapor prevents the sample from charging by carrying excess charge off into the gas phase, and water molecules also contribute to the secondary electron cascade measured by the detector. A schematic of the ESEM is shown in Figure 15.
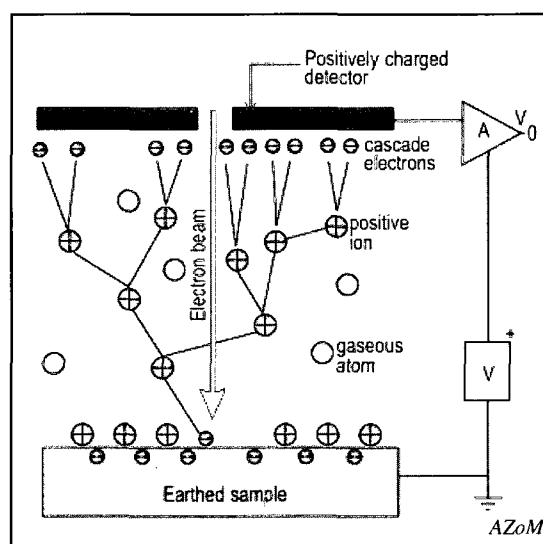
Figure 15. Schematic of environmental scanning electron microscope (ESEM).

Samples were also characterized by X-ray photoelectron spectroscopy (XPS, Phi Quantera) in order to analyze the elemental composition of the nanorod films' surfaces, *e.g.,* to determine whether carbon impurities are removed by plasma cleaning.

Substrate Bioconjugation and LSPR Sensing Measurements. A closed flow cell was assembled consisting of two glass slides (one coated with nanorods and one bare) separated by a 1.5 mm thick polydimethylsiloxane (PDMS) seal with a 1 cm x 2 cm slot that served as the flow volume. The clean glass slide had two drilled holes to connect the input and output flows. This flow cell was mounted vertically on an optical bench in between a quartz-tungsten-halogen light source with collimating lens, and a portable spectrometer (Ocean Optics, USB 4000). The 400 µL/minute flow rate was controlled by a syringe pump (NE1000, New Era Pump Systems). At the start of an experiment, the substrate was exposed to 0.1 M 2-(*N*-morpholino)ethanesulfonic acid (MES) buffer (Sigma, #M-0164) at pH 6.1 until the LSPR peak wavelength stabilized. The carboxyl groups on the mixed SAM were then activated by exposure to a 1:1 mixture of 0.1 M *N*-hydroxysuccinimide (NHS) (Sigma #130672) and 0.05 M 1-ethyl-[3-dimethylaminopropyl] carbodiimide (EDC) (Sigma #1769) in the MES buffer, followed by rinsing in the MES buffer. Then, the substrate was exposed to rabbit IgG (Pierce, #31235)) at about 1 µM in the MES buffer at pH 6.1, followed by a rinse with 0.05 M phosphate buffered saline (PBS) with 0.25 M NaCl at pH 7.6. Finally, either goat anti-rabbit IgG (Pierce, #31210) or goat anti-mouse IgG (Pierce, #31160) was flowed at the desired concentration in PBS buffer followed by a PBS buffer rinse at pH 7.6. The final step could be repeated more than once for successive tests of different secondary

antibodies. Absorbance spectra were collected with integration times of 5-20 ms, averaged for 30 s and recorded. Each spectrum was then analyzed in MATLAB with a Gaussian fit to monitor the peak wavelength, height, and width versus time.

Results and Discussion

The gold nanorods for this report were produced by seed-mediated, surfactant directed synthesis[64, 65], which has been widely applied to generate homogeneous gold nanorods with LSPR resonances in the visible and near-infrared. Slight variations in the reactant ratios yield a variety of other anisotropic shapes[64]. There are two main procedures for this process, a low-yield method that uses citrate-stabilized gold colloid as a starting point and results in penta-twinned crystal nanorods, and a high-yield method that begins with CTAB-stabilized colloid and results in single-crystal nanorods[66]. For our purposes, we chose the latter, high-yield method. In this process, gold colloid seeds are first synthesized by reducing gold chloride with sodium borohydride in the presence of a surfactant, CTAB. Then the seeds are added into a growth solution containing ascorbic acid, silver nitrate, and more gold chloride and CTAB. It is thought that the small gold colloid particles are coated with a CTAB bilayer, and when a defect forms in that bilayer, gold ions begin to reduce onto the surface at that point and the particle grows into an elongated structure[67, 68]. (See Figure 16.)

1. CTAB-capped gold seed particles grow by reduction of Au+ on their surface while surrounded by a surfactant bilayer. The bilayer regulates the growth rate.

CTAB   Br-   3. Anisotropic growth produces elongated gold nanorods in high yield.

2. A defect forms on the nanoparticle with poor surfactant binding to create anisotropic growth.
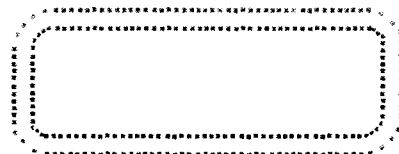
Figure 16. Surfactant-directed synthesis of gold nanorods.

The typical size of nanorods synthesized by this method under our conditions is 15 x 50 nm. A TEM image showing the structure of gold nanorods can be seen in Figure 17.

50 nm
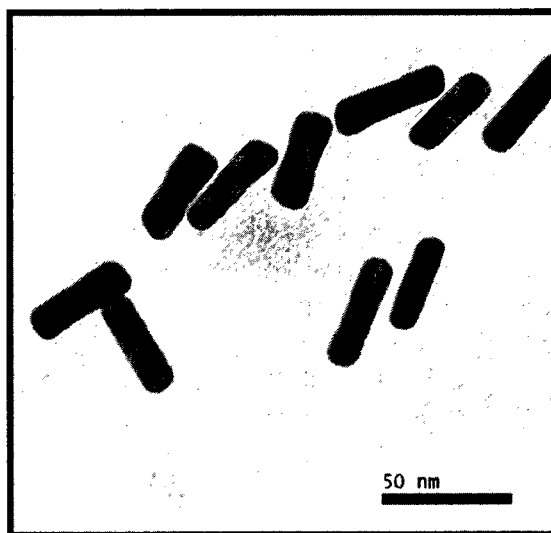
Figure 17. TEM image showing the structure of gold nanorods.

Chemical manipulation of nanorods is somewhat more complicated than that of classic citrate-stabilized gold colloid[69]. In surfactant directed synthesis, the CTAB acts as

both the source of anisotropic growth and the stabilizer[70]. The CTAB bilayer around the nanoparticles is clearly bound in a weak manner since a reduction of the CTAB concentration to below 1 mM, a concentration greatly in excess of that required to coat the nanoparticles, causes aggregation[71]. However, the particles can be stabilized by displacing the CTAB with a thiol terminated polyethylene glycol (PEG)[63]. (See Figure 18.)
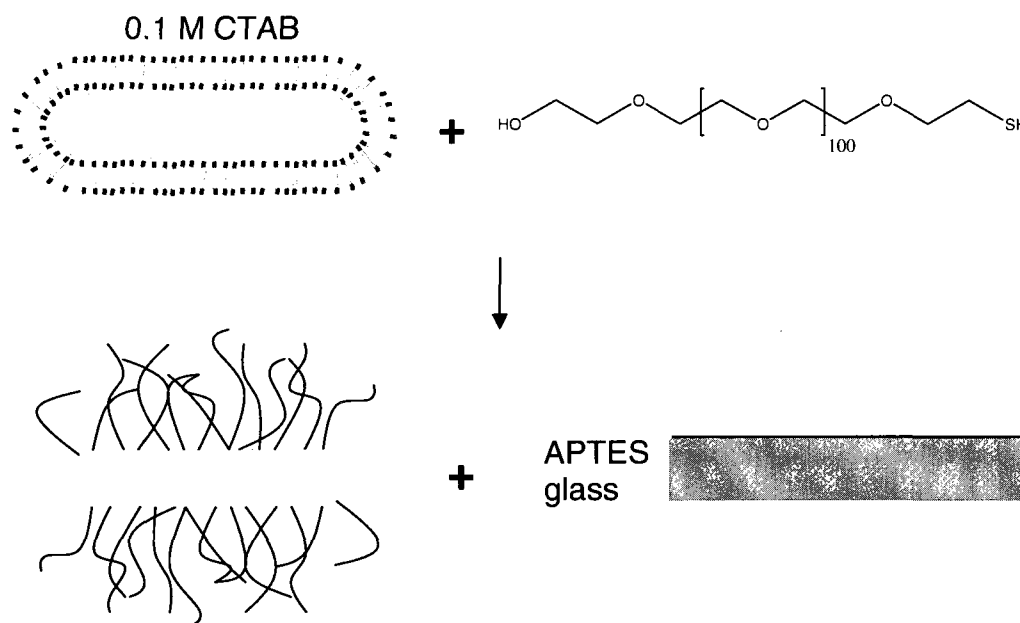
Figure 18. PEGylation of gold nanorods.

Once PEGylated, the nanorods can be transferred to solutions devoid of PEG or other stabilizers. PEGylation allowed bioconjugation of the nanorods in solution and processing of nanorods into well-ordered films. Figure 19 displays such a film, demonstrating the uniformity of deposition. The nanorods are randomly oriented, but the density is quite uniform and the particles are well separated, due to the PEG surrounding the particles upon deposition.
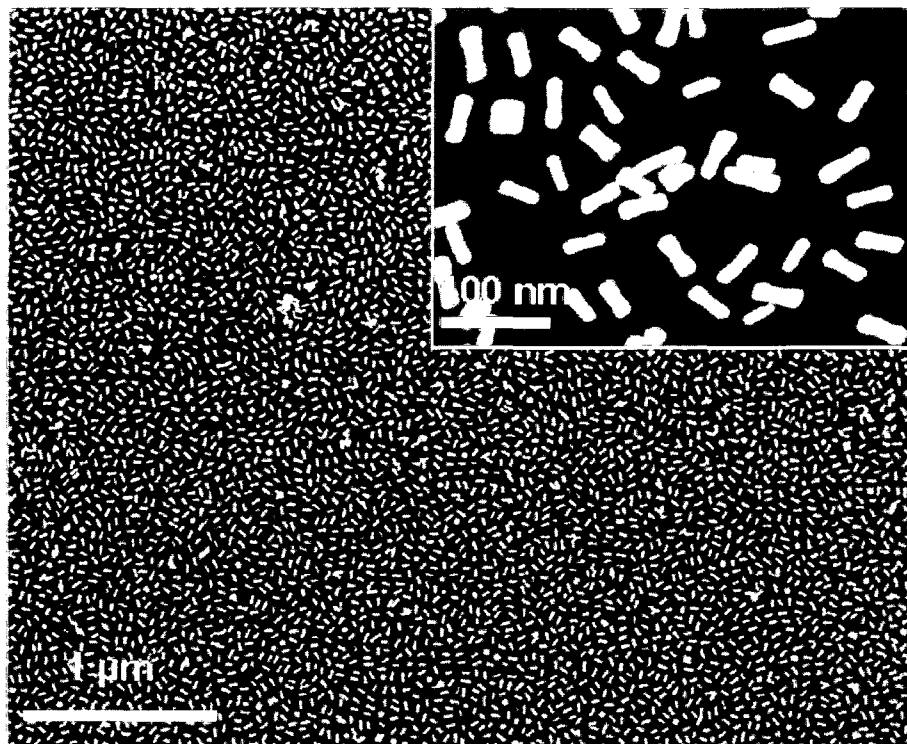
Figure 19. SEM image of a self-assembled nanorod film.

These films can cover the area of an entire microscope slide, and are visible to the eye as a purplish color. (See Figure 20a.) Their absorption spectrum is similar to that for the nanorods in solution (for example, Figure 5b), but the total signal is lower, as it is the absorbance of only one layer of particles (Figure 20b).
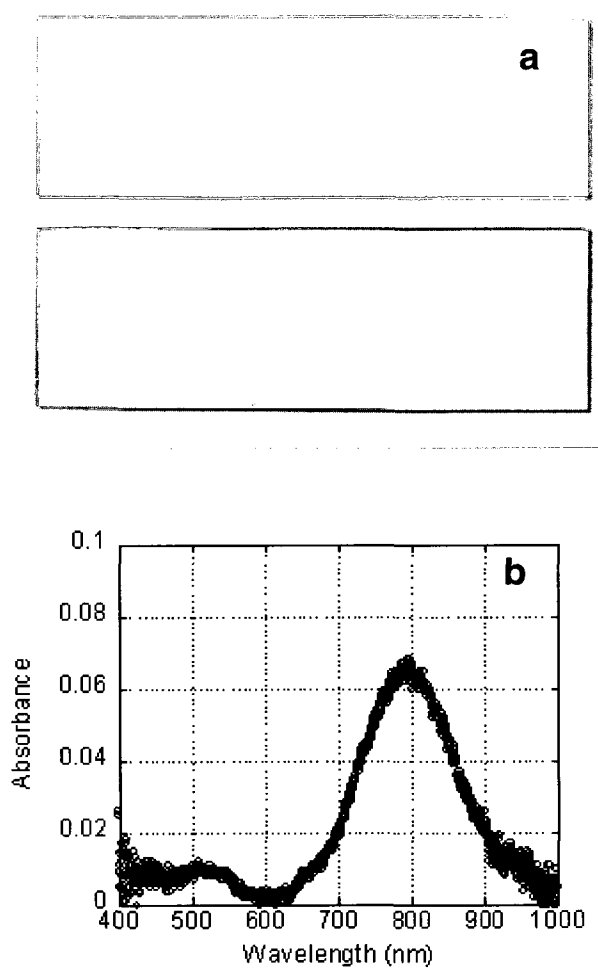
Figure 20. (a) Glass microscope slides before and after nanorod film deposition. (b) Absorbance spectrum of the nanorod film.

After particle deposition, the substrates were plasma cleaned to remove all PEG and other organic material, leaving only the thin APTES layer between the gold particle and glass slide. X-ray photoelectron spectroscopy (XPS) was carried out to confirm that carbon was removed from the surface. (See Figure 21.)
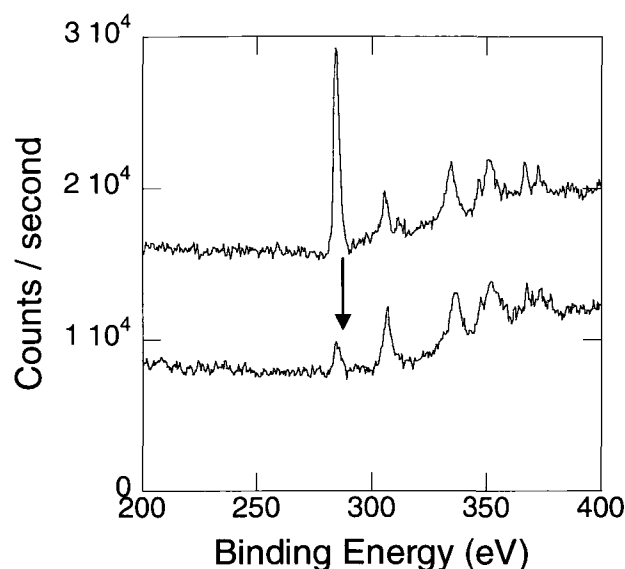
Figure 21. XPS measurements before (top) and after (bottom) plasma cleaning show that carbon
is removed from the nanorod film. (Carbon peak is marked with an arrow.)

Our initial attempts to use the PEGylation and bioconjugation protocols cited above

for LSPR sensing produced shifts in response to binding, but did not yield the correct

equilibrium binding constant for antigen/antibody interactions. Therefore, we adopted a

surface chemistry based on self-assembled monolayers (SAMs, see Figure 23)[72, 73]. First,

the nanorod substrates were treated with oxygen plasma to remove the PEG and expose a

clean gold surface. (The plasma presumably does not etch the APTES linkages holding

the   nanorods   to   the   glass   substrate.)   Once   cleaned,   mixed   SAMs   of

mercaptohexadecanoic acid and mercaptoundecanol were formed on the nanoparticles.

Since SAMs on nanoparticles larger than 4 nm in diameter have been reported to exhibit

behavior similar to those on planar surfaces[74], the nanorods can be thought of as planar

surfaces in terms of their surface chemistry.

The sensitivity of the SAM-coated nanorod substrates to changes in the refractive

index was checked by measuring the LSPR spectral extinction in four different dielectric

media: air, water, ethanol, and formamide (Figure 22). This yielded a refractive index sensitivity of 170 nm per refractive index unit (RIU). While this sensitivity is not exceedingly high as compared to those in other reports[75] (see Table 1 for a comparison) the resonances are fairly narrow with a full width at half-maximum of 125 nm in water. The resulting figure of merit (sensitivity/line width)[13] for these sensors is 1.3, which is similar to other reports on nanoparticle ensembles[75].
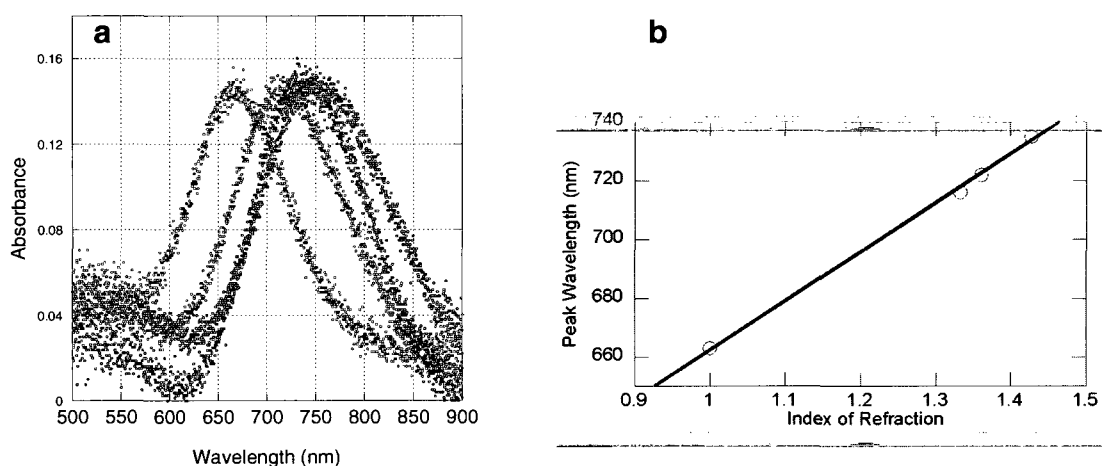
Figure 22. Characterization of the LSPR sensitivity to refractive index of the nanorod films: (a) Spectra of a nanorod film in four dielectric media. (b) The slope of the line yields a sensitivity of 170 nm/RIU.

The SAM is strongly bound to the nanorods via a gold-thiol bond, exposing the alcohol and carboxyl functional groups to the solution. (See Figure 23.) The mixed SAM used was chosen to reduce steric hindrances among protein molecules binding to the SAM layer.
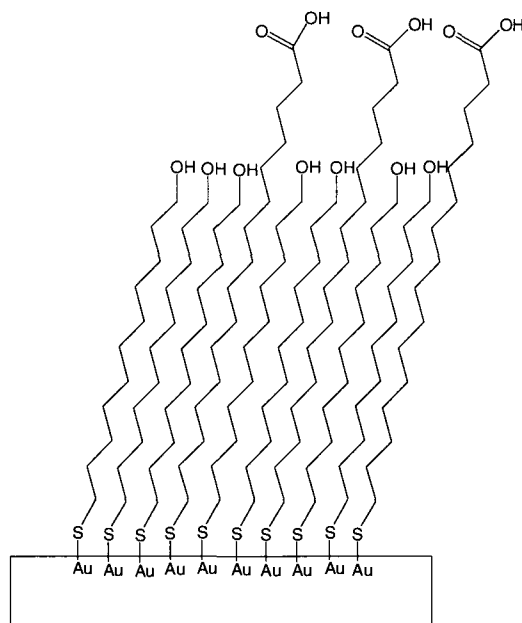
Figure 23. The mixed SAM made up of mercaptoundecanol and mercaptohexadecanoic acid.

Proteins are linked to the carboxyl-terminated SAM molecules via a well known carbodiimide chemistry procedure. In the original version of this reaction, 1-ethyl-[3-dimethylaminopropyl] carbodiimide (EDC) reacts with the carboxyl-terminated molecule at low pH, acting as a placeholder. When the protein is added, it replaces the EDC, forming an amide bond to the SAM. (See Figure 24a.) The intermediate formed in this version of the procedure is very short-lived (only a few seconds), so in practice a slightly more complicated process is used. In this case, a second placeholder molecule, *N*-hydroxysuccinimide (NHS) is used, which produces a longer-lived intermediate, useable for several minutes. (See Figure 24b.) Because they end as byproducts (in slightly-altered form), rather than being incorporated into the final complex, EDC and NHS are known as zero-length cross-linkers.
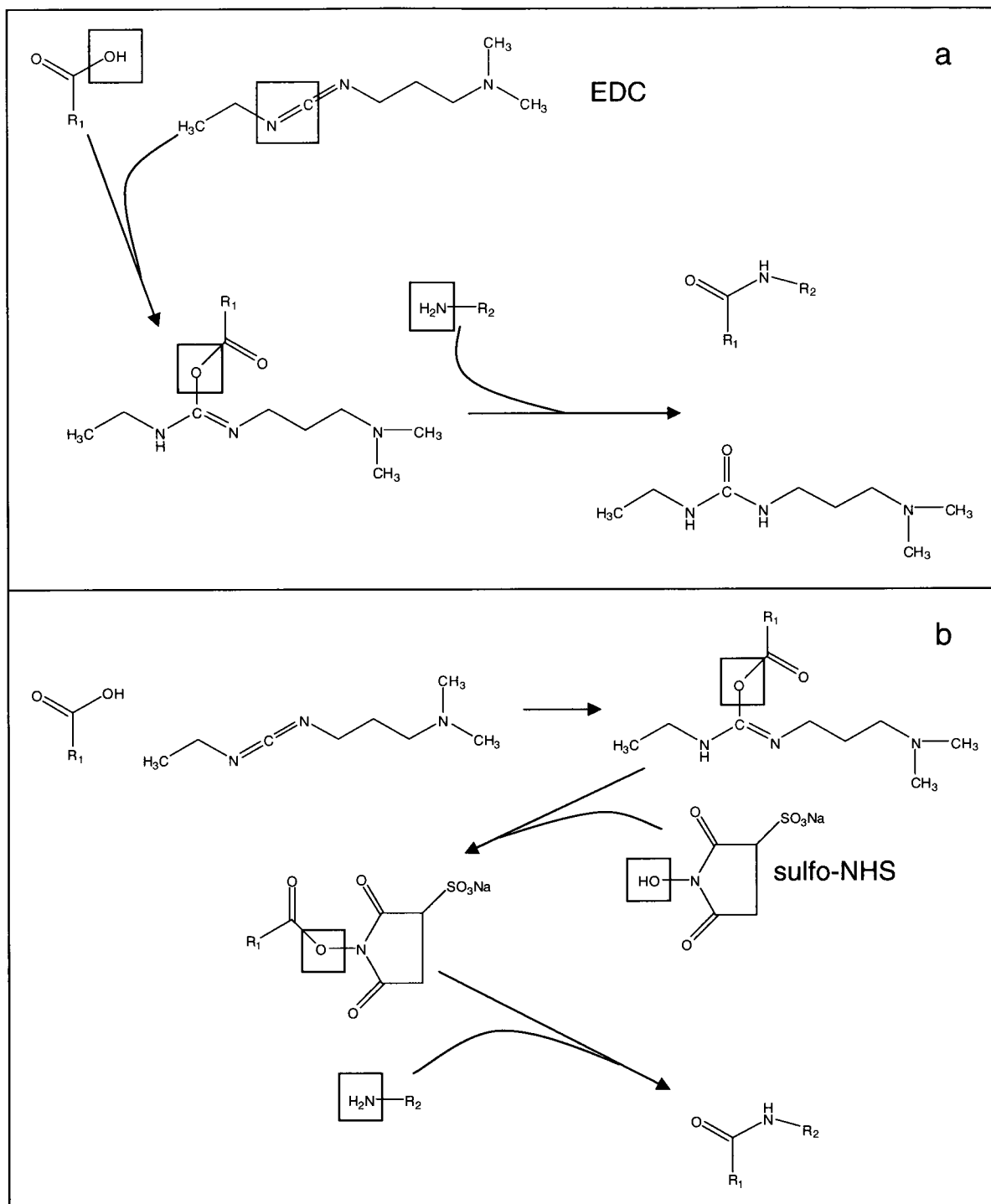
Figure 24. Carbodiimide cross-linking chemistry. (a) The simple EDC reaction. R1 represents the SAM molecule; R2, the protein. (b) Full NHS-EDC reaction.

The nanorod substrates were tested as LSPR sensors in the flow cell by first activating the carboxylic acid groups on the SAM *via* the carbodiimide chemistry

described above[69]. Rabbit IgG was coupled to the SAM to serve as a capture antibody, so that the binding of specific and nonspecific antibodies could be studied. The LSPR peak wavelength throughout such a reaction is displayed in Figure 25a. The entire experiment was carried out in a flow chamber, depicted in Figure 25b. First, the peak wavelength was allowed to stabilize against solvent annealing under a flowing buffer (not shown)[21]. Exposure of the activated carboxy-terminal nanorod SAM substrate to rabbit IgG produced the expected red shift of the LSPR peak wavelength due to IgG binding. The subsequent blue shift occurred during rinsing and was likely due to the removal of physisorbed rabbit IgG. Exposure to 30 nM goat anti-rabbit IgG caused a further red shift as the specific secondary antibody bound the capture antibody on the sensor. Then, the substrate was rinsed and unbinding of the secondary antibody was monitored *via* a blue shift. The final goat anti-rabbit IgG step was repeated three times to demonstrate substrate stability and reproducibility of the molecular interaction. The on and off rates for antibody binding were fit with a standard 1:1 first-order kinetics binding model[76] which yielded $k_{off} = 6.5 \times 10^{-5}$ s^{-1} and $k_{on} = 1.3 \times 10^{5}$ M^{-1}s^{-1}, resulting in an equilibrium constant of $K_{eq} = 2.0 \times 10^{9}$ M^{-1}. This is a typical equilibrium constant for an antibody-antigen interaction[76], and is the first measurement of the equilibrium constant from kinetic rates by LSPR sensing. This measurement was repeated several times, yielding equilibrium constants between 2×10^{8} M^{-1} and 2×10^{9} M^{-1}. The additional data and fits can be found in Appendix 1. The rates presented here match well to those observed for antibody-antigen binding in SPR.
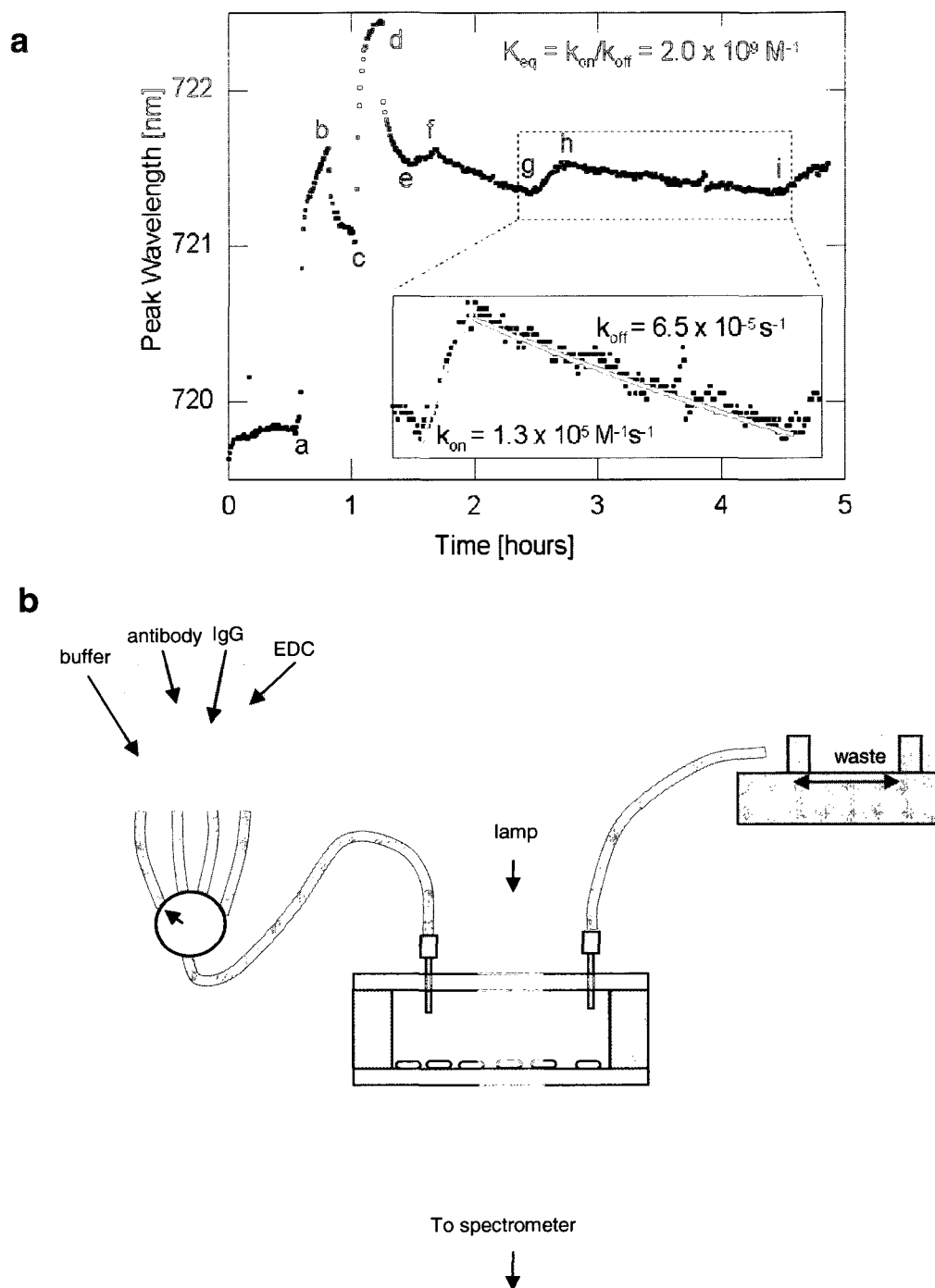
Figure 25. (a) Immunoassay with kinetic data fits. The peak absorbance wavelength was measured *versus* time as the various solutions flowed over the substrate in a continuous experiment. Initially, the substrate was under a pH 6.1 buffer solution. At step a the substrate was exposed to a mixture of NHS and EDC, activating the SAM for protein binding. At step b, the substrate was rinsed with pH 6.1 buffer. At step c, rabbit immunoglobulin (IgG) was introduced. At step d, the substrate was rinsed with pH 7.6 buffer. At step e, it was exposed to 30 nM goat antirabbit IgG. At step f, it was again rinsed in pH 7.6 buffer. At steps g through i, these final steps were repeated twice more. (b) Schematic of the flow cell and white-light extinction setup.

Figure 26 illustrates a similar assay that tests the nanorod LSPR sensor's immunospecificity. The nanorod conjugation with rabbit IgG was carried out exactly as described above, but the substrate was then exposed to 10 nM goat anti-mouse IgG as an analyte. As expected, there was very little binding of the nonspecific secondary antibody. When the specific secondary antibody was added in a subsequent step, significant binding was observed. This explicit demonstration confirms that the LSPR sensor retains the specificity of the capture antibody.
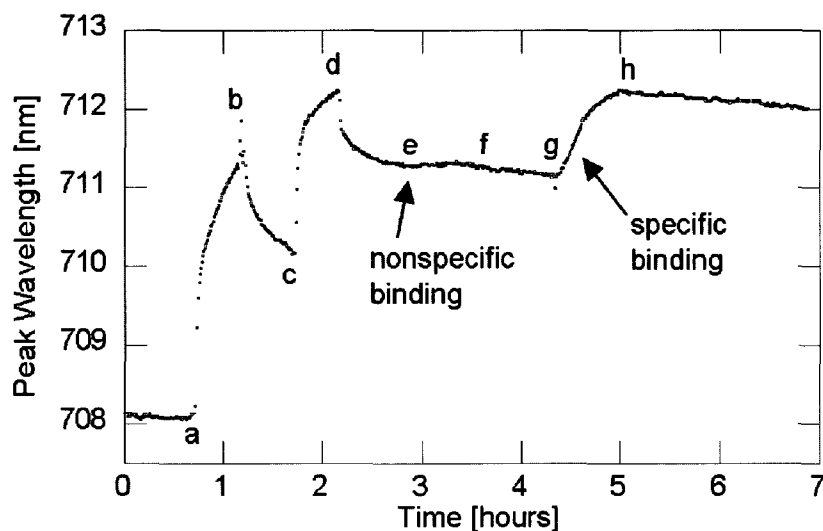
Figure 26. Demonstration of sensor specificity. Steps **a** through **d** are as in Figure 25. In step **e**, the substrate was exposed to 10 nM goat anti-mouse IgG, a nonspecific secondary antibody to the rabbit IgG. The binding is extremely weak. Step **f** is a buffer rinse. In step **g**, the substrate was exposed to 10 nM goat anti-rabbit IgG, and strong, specific binding was seen. Step **h** is a buffer rinse.

In addition, the detection sensitivity was measured. In Figure 27, the nanorod conjugation with rabbit IgG is again the same as in Figure 25, but in this case, the concentration of goat anti-rabbit IgG was raised in subsequent steps. When the antibody was added at a concentration of 100 pM, there was no measurable response. When the

concentration was increased to 1 nM, the peak began to shift, with a slope of 0.076 +/-

0.005 nm/hour. When the concentration was again increased to 10 nM, the slope, which

should be proportional to concentration (to first order), also increased tenfold, to 0.76 +/-

0.007 nm/hour. From this, we found that the limit of detection of this sensor over a

reasonable time scale is about 1 nM.
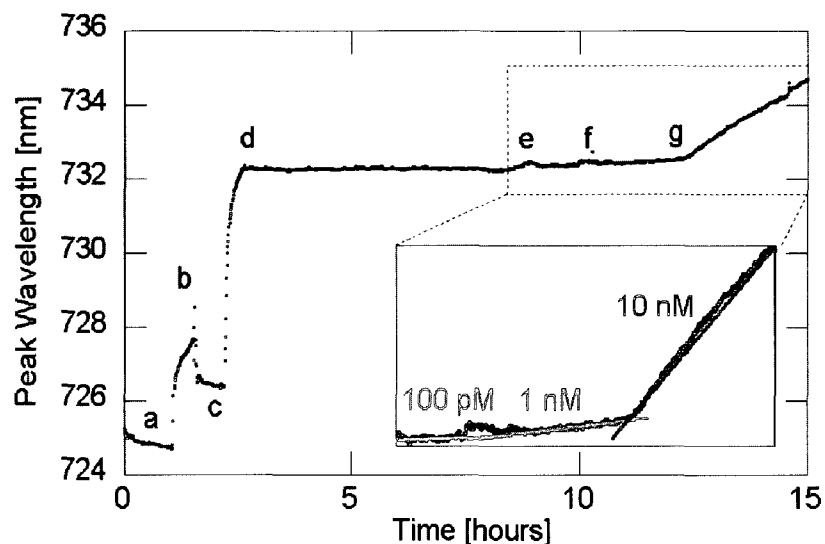
Figure 27. Test of sensor sensitivity. Steps **a** through **d** are as in Figure 25. In step **e**, the specific antibody (goat anti-rabbit IgG) was added at a concentration of 100 pM. The concentration was increased to 1 nM (at **f**) and 10 nM (at **g**). The inset shows linear fits to the binding curve.

Figure 28 illustrates the relationship between the LSPR shift due to the capture

antibody binding and the LSPR shift due to analyte antibody binding over several

experiments using different substrates. The linear relationship demonstrates that the

results are reproducible and consistent from experiment to experiment. Given that the

nanoparticle substrate properties were similar, the variation in signal is most likely due to

variation in the yield of capture antibody conjugation.
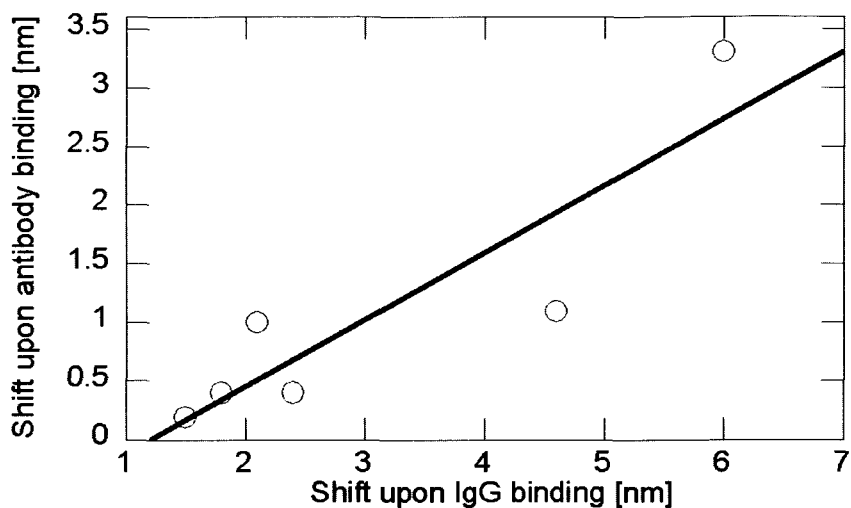
Figure 28. Comparison of LSPR shifts upon initial protein binding and specific antibody binding.

Most recent work on LSPR sensors has focused on maximizing the dielectric sensitivity by optimizing the nanoparticle shape[18, 24, 75, 77, 78]. While this is certainly advantageous, it is not a complete solution to extending LSPR applications in science and technology. Other significant issues are the stability and availability of the sensor substrates, their chemical interface with the analyte, and the need for quantitative dynamic measurements. Here we have addressed these issues by fabricating LSPR substrates based on chemically synthesized gold nanorods with no lithographic steps and by exploiting standard techniques in self-assembly and bioconjugate chemistry. The resulting substrates are highly stable, as seen in the approximately 15-hour experiment in Figure 27. Also, the substrates can be plasma cleaned and reused, with some having undergone roughly 20 such cycles in our laboratory. Although the nanorod substrates are not as sensitive as some other LSPR geometries, their performance is comparable to dynamic SPR measurements in immunoassays. Such immunoassays may prove to be a significant application of LSPR sensing given the need for broadly available high-

throughput screening in fields such as proteomics, systems biology, and *in vitro* diagnostics.

In summary, gold nanorod LSPR sensor substrates were fabricated by self-assembly for the study of biomolecular interactions. Through careful control of their surface chemistry, the nanorods were conjugated with capture antibodies which enabled immunospecific detection of secondary antibodies. Correct binding kinetics was measured, thus demonstrating that the nanorod LSPR sensor can monitor real-time dynamic interactions in a similar manner to SPR. In combination with recent reports on multiplexed nanorod LSPR sensors and high throughput LSPR assays, these substrates may help to expand LSPR sensing technology more broadly.

IV.   Improving the Sensitivity of the LSPR Immunoassay

Background

In order for LSPR sensing to be useful in clinical diagnostics and research applications, it must be able to compete with ELISA, which means the sensitivity must be improved. Strategies include optimizing the surface chemistry and modifying the particle shape.

Because the LSPR sensing volume is localized close to the particle surface, any surface conjugation strategies that bring the target molecule closer to the gold surface ought to improve the sensitivity of target detection. This strategy can be applied to the SAM layer on the particles, or to the capture layer itself. In order to create a thinner capture layer, aptamers may be used instead of antibodies. Aptamers are short sequences of single-stranded DNA that, due to their conformation, have a high binding affinity for a specific protein. They are discovered through DNA library screening processes[79]. One of the best-known aptamers is the thrombin-binding aptamer, pictured in Figure 29. (Thrombin is a seroprotein found in human blood plasma that is important in clot formation.)

Figure 29. The thrombin-binding aptamer (blue) attaches to its binding site on thrombin (purple).

Aptamers have attracted a great deal of interest due to their potential as "artificial antibodies," combining high specificity for their protein targets and the chemical robustness of single-stranded DNA. Label-free protein detection with kinetics by aptamers has already been shown in SPR studies[80, 81]. Because of their relatively small size (2-3 nm), aptamers are especially promising as a capture molecule for LSPR sensors, since the target molecules will bind closer to the gold surface, in the highly sensitive sensing volume of the particles.

LSPR sensitivity can also be improved through choice of particle shape. As compared to nanorods, gold bipyramids have a narrower LSPR peak and a higher sensitivity to the surrounding refractive index.

Methods

Gold Bipyramid Synthesis. All solutions were prepared fresh for each synthesis using deionized (DI) water, except for the hydrogen tetrachloroaurate(III) (Sigma, No.520918), which was prepared as a 28 mM stock solution from a dry ampule and stored in the dark. First, sodium citrate-stabilized gold seed particles were prepared for the synthesis of gold bipyramids. Typically, a 20 mL solution of 0.125 mM hydrogen tetrachloroaurate(III) and 0.25 mM sodium citrate (Fisher, No. S279) were prepared and mixed briefly. Next, 0.3 mL of a fresh aqueous 10 mM $NaBH_4$ (Acros, No. 18930) solution prepared at room temperature was added, followed by mixing for 2 min. The resulting gold seed solution was kept at room temperature for at least 2 h for complete reaction. Then, the dark pink seed solution was stable and usable for gold bipyramid growth. Next, 0.5 mL of 10 mM hydrogen tetrachloroaurate(III) and 10 mL of 100 mM cetyltrimethylammonium bromide (CTAB) (Sigma, No. H9151) were mixed with 0.1 mL of 10 mM silver nitrate (Acros, No. 19768) for the preparation of the growth solution. Then, 0.2 mL of 1.0 M hydrochloric acid (Hampton Research, No. HR2-581) and 0.08 mL of 100 mM L-ascorbic acid (Fisher, No. A61) were added to the solution in order. Finally, the seed solution was added to the growth solution. The volume of seed solution was varied between 15 and 50 μL to synthesize different sizes of gold bipyramids. These solutions were kept at 28 °C for several hours. During this time, the color changed gradually from almost clear to dark pink, with most of the color change occurring in the first hour. The PEGylation and substrate fabrication procedures for bipyramids, as well

as subsequent characterization and immunoassay procedures are the same as those described in the previous chapter for gold nanorods.

Results and Discussion

Aptamer-Based Assay. A nanorod film immunoassay was developed for an aptamer-protein system. Gold nanorod films were prepared as in Chapter III and functionalized with thrombin-binding aptamers prepared with thiol-modified single-stranded DNA. (Note: this work was carried out with our collaborators from the Spivak group at Louisiana State University.) Real-time, label free thrombin detection experiments were carried out for a variety of analyte concentrations, in the same manner as for the antibody-antigen system. In Figure 30, the kinetics of thrombin association and dissociation are shown for a sample containing human thrombin at a concentration of 10 nM in PBS buffer. The rates measured were $k_{on} = 9140 \text{ M}^{-1}\text{s}^{-1}$ and $k_{off} = 6.6 \times 10^{-4} \text{ s}^{-1}$. The equilibrium binding constant determined by taking the ratio of these rates was $K_{eq} = 1.33 \times 10^{7} \text{ M}^{-1}$. This binding constant is two orders of magnitude weaker than that measured for antibody-antigen interactions, which is consistent with known data on aptamers. In Figure 30b is a comparison of this result with that from the antibody-antigen system from the previous chapter in terms of LSPR shift per hour per molecular weight of the target. The antibody gives an intitial sensor response rate of 5.4×10^{-6} nm/MW·hr, and the aptamer gives 5.2×10^{-5} nm/MW·hr, an improvement by almost a factor of ten. (The molecular weight of thrombin is 72 kDa and that of IgG is about 150 kDa.) Because of the aptamer's small size (only ~20 bases of single-strand DNA), the

target is able to approach much closer to the nanoparticle surface, in the localized sensing volume, and produce a much larger signal.
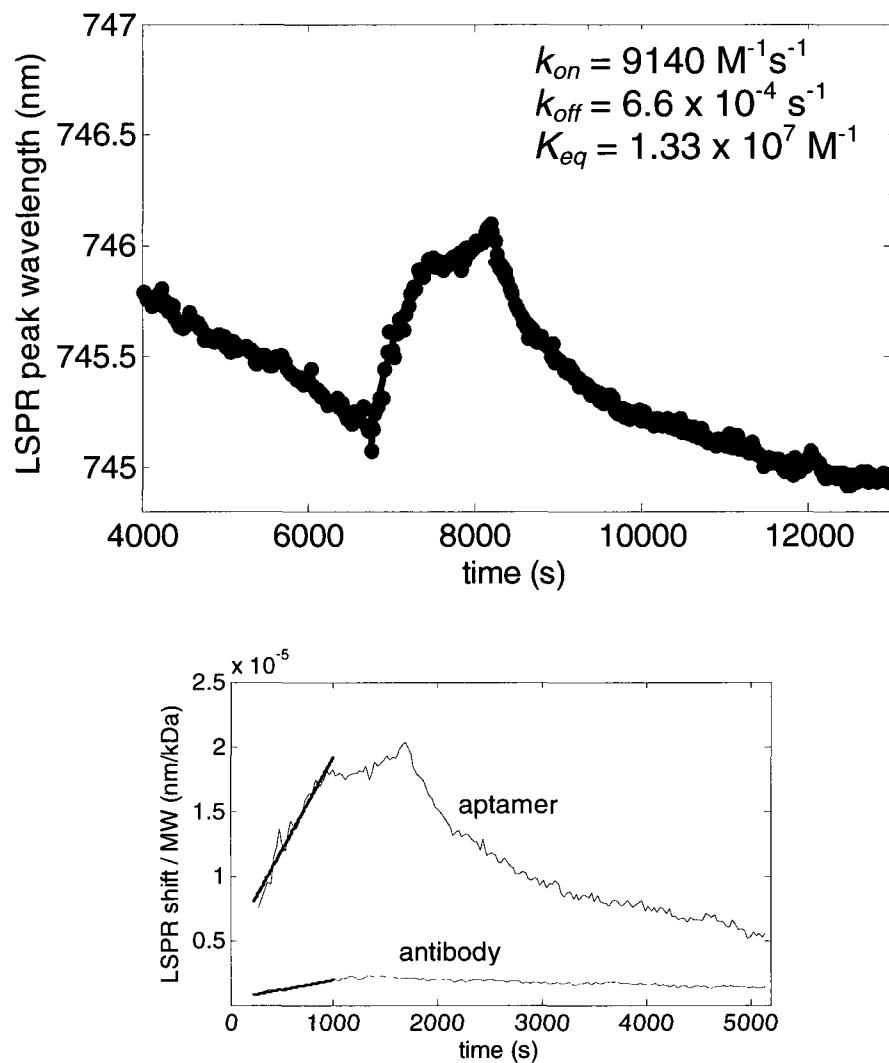
Figure 30. (a) Kinetics of aptamer-thrombin binding for 10 nM thrombin. Fits are to a first-order binding kinetics model. (b) Comparison of LSPR signal from antibody-antigen and aptamer-protein systems.

A dose-response experiment was also carried out, in which the thrombin concentration that the aptamer-functionalized nanorod substrate was exposed to was

ramped up from 1 nM to 1 μM. (See Figure 31.) The response is greatest between 1 and

50 nM and then begins to level off, consistent with the measured equilibrium constant.
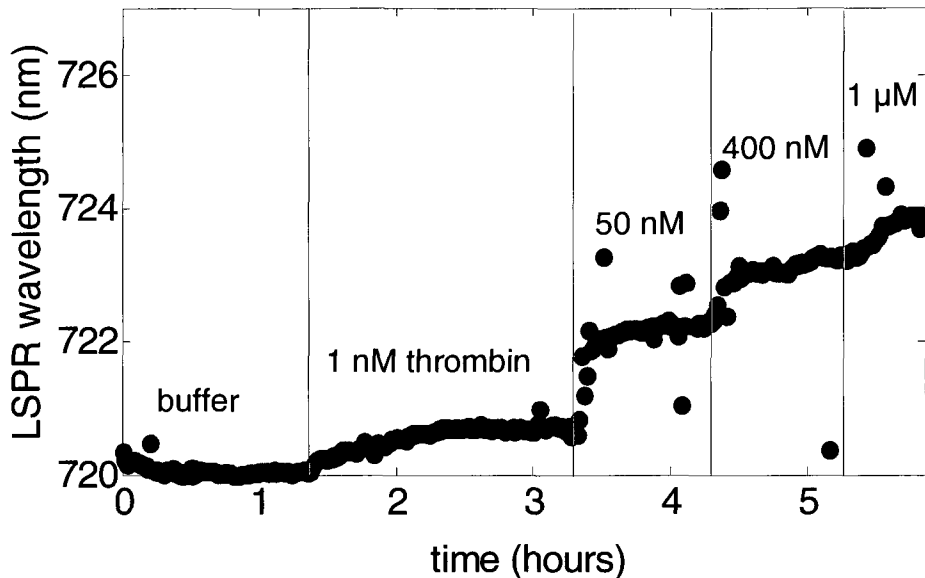
Figure 31. Dose-response experiment for the thrombin-binding aptamer on a gold nanorod substrate.

LSPR Immunoassay with Gold Bipyramid Substrates. In a further effort to improve

the detection sensitivity of the LSPR immunoassay, substrates were fabricated with gold

bipyramids[66], which have a narrower LSPR peak and higher refractive index sensitivity.

Gold biypramids of varying size and aspect ratio were synthesized to determine the

optimum size for LSPR sensing. A TEM image of a typical gold bipyramid having a tip

radius of curvature of less than 5 nm is shown in Figure 32a. The corresponding electron

diffraction pattern, shown in Figure 32b, is consistent with a pentatwinned structure as

described in the original report.

A

50 nm

B
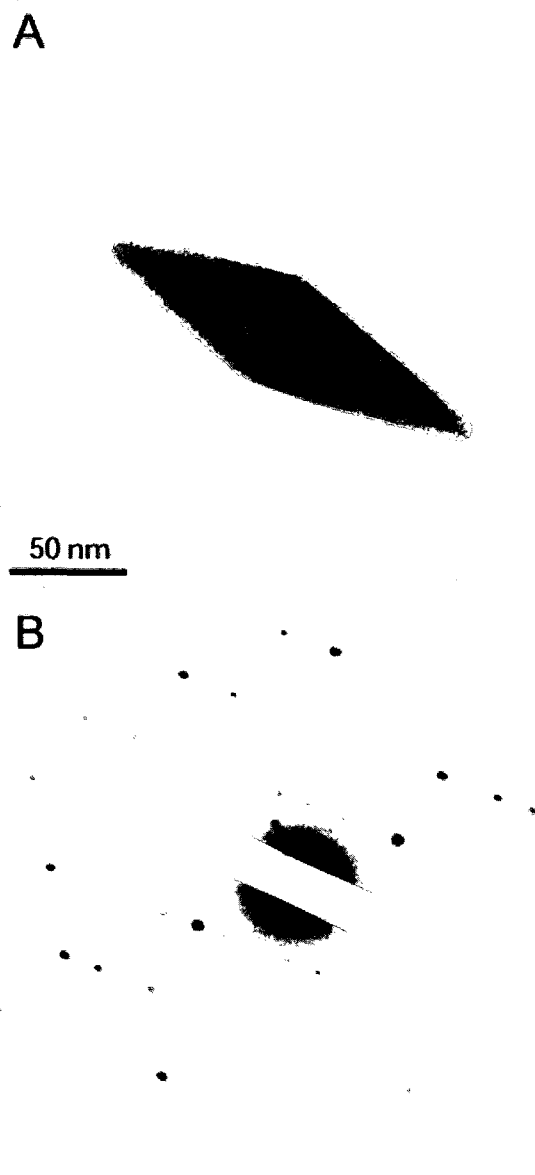
Figure 32. (a) TEM image of a PEGylated gold bipyramid. (b) Electron diffraction pattern of a gold bipyramid, consistent with a pentatwinned crystal structure. Images courtesy of Sean Lee.

To synthesize different sizes of gold bipyramids, four different volumes of the seed solution (15, 20, 35, and 50 µL) were employed. The extinction spectra of the resulting CTAB-stabilized gold bipyramid solutions are shown in Figure 33. With decreasing seed volume, the bipyramid spectra red shift because of their larger size, and the peak height drops because of the smaller number of particles.
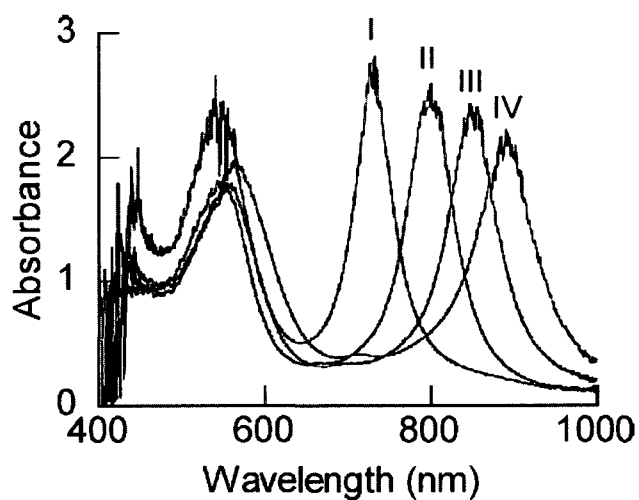
Figure 33. Spectra of four bipyramid samples of varying particle size.

The gold bipyramids were processed into films as previously described for gold nanorods. An ESEM image and an extinction spectrum of a typical bipyramid film are shown in Figure 34. The spectrum is sufficiently strong to monitor peak wavelength shifts because of molecular binding onto the nanoparticle surface. The synthesis procedure yields both bipyramids and nanospheres, as can be seen in the ESEM image in Figure 34a.
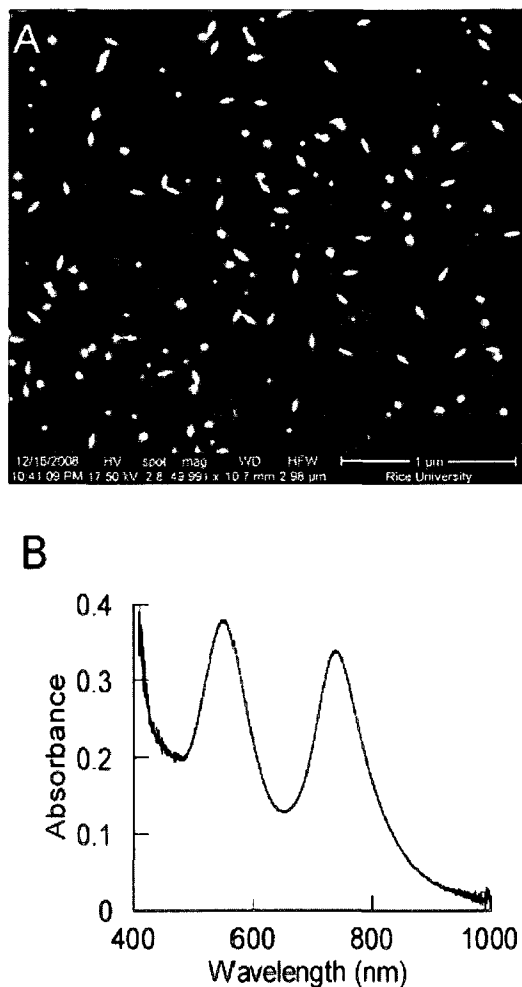
Figure 34. (a) Wet-mode ESEM image of a film of gold bipyramids on glass. (b) Absorbance spectrum of a bipyramid substrate.

The yield of gold bipyramids on the glass surface, defined as the percentage of total particles that are bipyramids rather than spheres, was quantified by atomic force microscopy (AFM, Nanoscope IV), and electron micrographs were obtained using an FEI Quanta 400 environmental scanning electron microscope (ESEM) in wet-mode. Table 3 summarizes the sizes, aspect ratios, yields on the surface, and longitudinal LSPR peak wavelengths and widths of substrates made from each bipyramid sample.

	NR	BP I	BP II	BP III	BP IV
Seed Volume (µL)	—	50	35	20	15
BP Yield	—	22%	22%	21%	23%
Length/ Diameter (nm)	50/15	108 / 44	137 / 51	162 / 57	185 / 58
Aspect Ratio	3.3	2.5	2.7	2.8	3.2
Peak wavelength (nm)	760	730	800	850	900
Sensitivity (nm/RIU)	170	288	327	346	381
FWHM (nm)	125	74	89	100	100
FOM	1.3	3.9	3.7	3.5	3.8

Table 3. Summary of bipyramid properties. Table courtesy of Sean Lee.

The refractive index sensitivities of the bipyramid substrates with different aspect ratios were investigated by measuring the LSPR peak wavelength shift in various solvents. The LSPR spectra of the gold bipyramid substrates were measured in water (n = 1.333), acetonitrile (n = 1.3441), ethanol (n = 1.361), dimethylformamide (DMF, n = 1.431), and toluene (n = 1.497). As seen in Figure 35, the LSPR peak red shifts with increasing index. (The detailed spectra can be found in Appendix II.) The refractive index sensitivities of the samples were determined from the slope of the lines in Figure 35. The sensitivity was found to increase with particle aspect ratio. In addition, the figures of merit (FOM) were calculated as sensitivity divided by the LSPR full width at half-maximum (fwhm). The bipyramid substrates have higher FOM values of 3.5-3.9 compared to gold nanorod substrates. As seen in Table 3, the largest bipyramid has the

highest sensitivity, but the smallest has the highest figure of merit because of its narrow

line width.
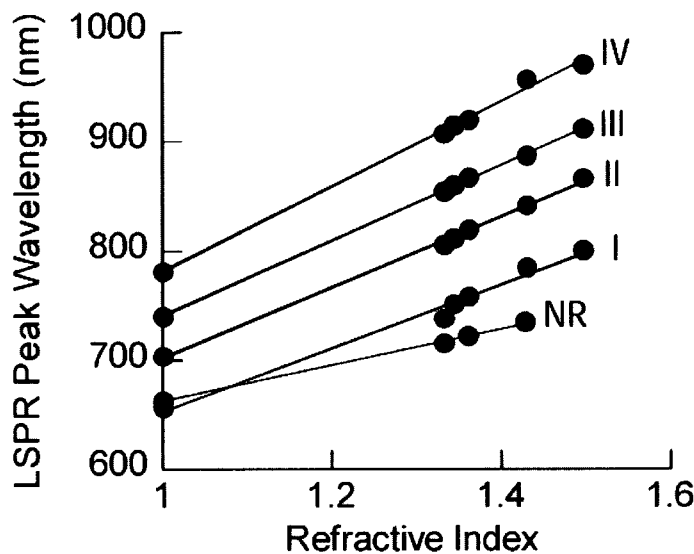
Figure 35. Refractive index sensitivity of gold bipyramids of various sizes on glass substrates. The samples I through IV are labeled as in Figure 33. Data courtesy of Sean Lee.

In addition to their higher bulk refractive index sensitivity, bipyramids also possess

the advantages of monodispersity in terms of size and shape (resulting in the narrow

extinction linewidth) and sharp tips with potential for strong field enhancement[82]. It can

be shown by finite element method simulations that strong local electric fields can

contribute to the refractive index sensitivity of nanostructures[83]. Our results are in good

agreement with a recent report on the refractive index sensitivity of similar gold

bipyramid substrates[84].

To demonstrate the immunosensing capabilities of these substrates, a capture

antibody (rabbit IgG) was bound to a carboxy-terminal SAM on the bipyramid surfaces

by amide bond formation with a carbodiimide. The functionalized substrates were then

exposed to a solution containing the target antibody (goat anti-rabbit IgG), using the

methods described previously. By monitoring the optical extinction peak at the bipyramids' LSPR resonance throughout the target exposure and subsequent rinse, a real time immunoassay was performed. A section of the resulting sensorgram is shown in Figure 36. At the lowest concentration of target antibody (100 pM), there was no significant response from the sensor. At 1 nM, the extinction peak began to shift at a rate of 4.0×10^{-5} nm/s, and at 10 nM, the rate increased to 5.5×10^{-4} nm/s. Although the minimum detectable concentration stayed the same, these bipyramid peak shift rates are larger than those from the same experiment carried out on a nanorod substrate (2.1×10^{-5} and 2.1×10^{-4} nm/s, respectively) by a factor of 2, which matches well with the increase in refractive index sensitivity. Endpoint spectra from the sensor response can be found in Appendix II.
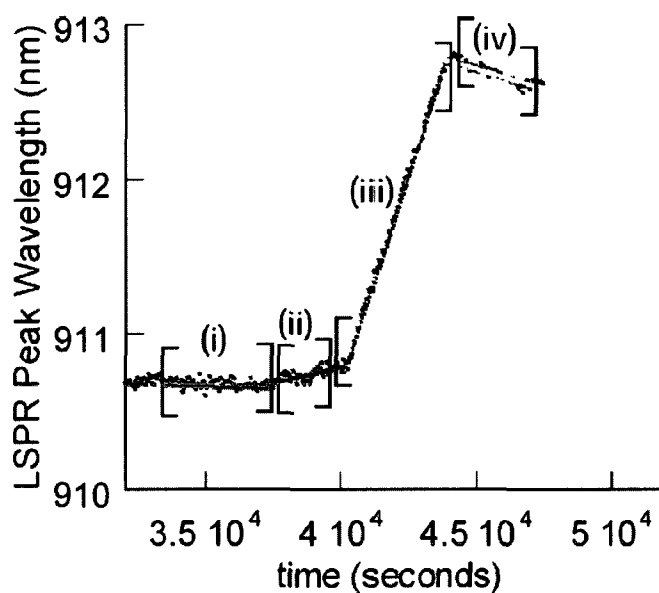
Figure 36. Immunoassay sensorgram. The dose response can be seen as the bipyramid substrate was exposed to target antibodies at 100 pM (i), 1 nM (ii), and 10 nM (iii). Kinetic rates of binding and unbinding were obtained from the 10 nM exposure (iii) and rinse (iv). Segments (i) and (ii) are linear fits, while the (iii) and (iv) are fits to the first-order binding kinetics model. This sensorgram yielded a binding rate of $k_{on} = 3.03 \times 10^{3}$ M^{-1} s^{-1} and an unbinding rate of $k_{off} = 3.56 \times 10^{-6}$ s^{-1}. The ratio of these gives an equilibrium constant of Keq) 8.51×10^{8} M^{-1}, which compares favorably with standard literature values for antibody-antigen bonds.

The LSPR sensor response in an immunoassay will depend on several factors in addition to the refractive index sensitivity of the nanoparticle. For example, conjugation chemistry for binding the capture antibody to the nanoparticle will affect the density of capture antibody and therefore target molecules on the nanoparticle surface. Furthermore, the conjugation strategy will affect the distance between the target molecule and the nanoparticle surface and therefore the size of the LSPR shift (as discussed below). To characterize the LSPR sensitivity in a real immunoassay, one can relate the measured LSPR peak shift to the parameters of a simple first-order molecular binding model used to describe the kinetics of the system. As discussed in the Introduction, according to the model, the concentration of capture-target antibody complexes formed on the surface evolves in time upon target exposure as:

$$[CT]_{surf}(t) = \frac{k_{on}[C]_{surf}[T]_{sol}}{(k_{off} + k_{on}[T]_{sol})}\left[1 - e^{-(k_{off} + k_{on}[T]_{sol})t}\right] \tag{29}$$

Here, C denotes the capture antibody, T the target antibody; k_{on} and k_{off} are the association and dissociation constants, and *surf* and *sol* denote surface and volume concentrations, respectively. Equation 29 can be expanded for short exposure times to yield the initial linear shift:

$$[CT]_{surf}(t) = (k_{on}[C]_{surf}[T]_{sol})t \tag{30}$$

If one assumes that the observed LSPR peak wavelength shift is proportional to the concentration of capture-target complexes near the nanoparticle surface, then Eqn. 30 can be written:

$$\Delta\lambda = K_{LSPR}(k_{on}[C]_{surf}[T]_{sol})t \tag{31}$$

The constant K_{LSPR} describes a nanoparticle substrate's performance in an immunoassay and has units of nm·μm^2 if the shift is given in nm and the capture antibody density on the nanoparticles is given in molecules/μm^2. For the bipyramid results in Figure 36, K_{LSPR} = 0.01 nm·μm^2 if one assumes approximately 20 active antibodies per bipyramid. This assumption is based upon an estimated particle surface area of 10,000 nm^2 and a surface area per active antibody of 100 nm^2, with a binding efficiency of 0.2, similar to results found on gold surfaces[85]. This constant reflects the effect of the nanoparticle refractive index sensitivity and antibody conjugation strategy on the immunoassay sensitivity. The value reported here cannot yet be compared to other LSPR sensor reports since real-time measurements are required.

To explicitly compare the sensing capability of the bipyramids to those of other plasmonic nanoparticles, a substrate was fabricated with a hybrid film containing three particle types: bipyramids, nanorods, and nanospheres. Figure 37a shows an ESEM image of the hybrid film on glass. The optical extinction spectrum of this substrate (Figure 37b) includes three well-separated peaks representing the three particle types, the spheres having an extinction peak near 580 nm, the nanorods near 700 nm, and the bipyramids near 950 nm. By tracking this spectrum in real time during an immunoassay experiment similar to that described above, it is possible to generate sensorgrams for each of the three peaks, seen in Figure 37c. Comparing these, it is clear that the bipyramids are the most sensitive, that is, give the largest extinction peak shift in response to the target binding. The relatively poor signal-to-noise ratio in these sensorgrams, and the apparent lack of signal for the nanorods and spheres, is due to the low density of each type of

particle on the hybrid substrate. The results for the hybrid substrate are summarized in

Table 4.
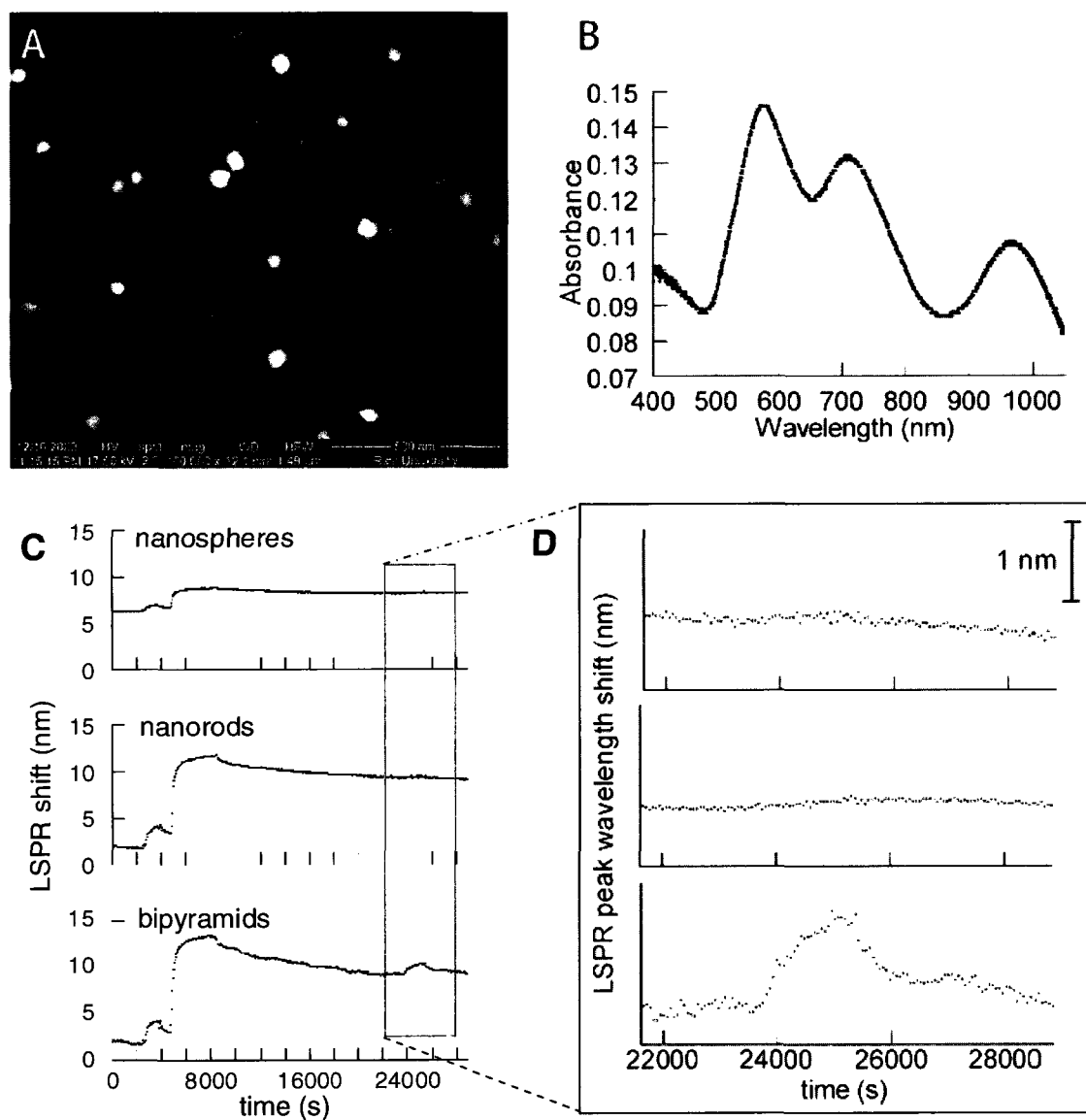
Figure 37. (a) ESEM image of the hybrid substrate containing gold nanospheres, nanorods, and bipyramids. (b) Optical extinction spectrum of the hybrid substrate. (c) Sensorgrams for each of the three particle types in the hybrid substrate immunoassay. (d) Zoom in on the target binding step for each particle type.

Particle	Total Response (nm)	Shift rate for 10 nM analyte (nm/hour)
Spheres (H)	0.4630	0.40
Nanorods (H)	0.6693	0.50
Bipyramids (H)	1.7433	4.7
Nanorods (previous data)	n/a	0.76

Table 4. Summary of results from the hybrid substrate including nanospheres, nanorods, and bipyramids. Data from regular nanorod substrates included for comparison.

Effect of SAM Length. A third strategy to improve the LSPR sensitivity to target binding was to decrease the target's distance from the gold particle surface by using a shorter SAM. Two bipyramid substrates from the same fabrication run were coated with carboxy-terminal SAMs of two different lengths: mercaptoundecanoic acid and mercaptohexadecanoic acid. The difference in thickness between these eleven and sixteen-carbon chains is approximately 7 Å. The same immunoassay experiment was then carried out on both substrates. The LSPR shift from the substrate with the shorter SAM was larger by 1 nm as seen in Figure 38. In addition, the initial sensor response rate from the mercaptohexadecanoic acid was 4.7 nm/h, and that from the mercaptoundecanoic acid was 6.1 nm/h, an improvement of 30%.
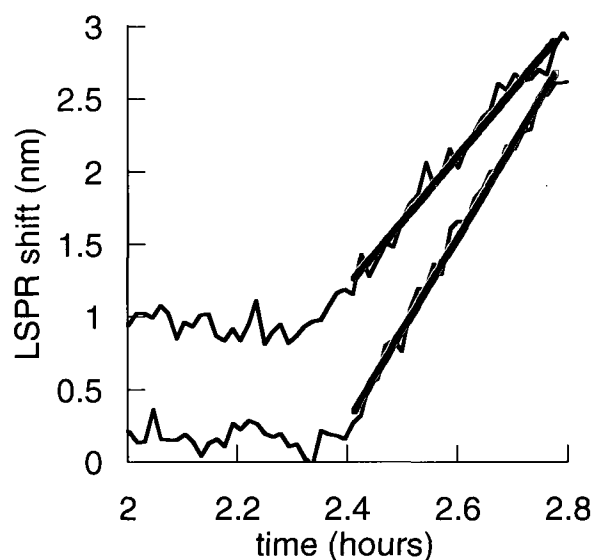
Figure 38. Comparison of the target antibody binding signal from bipyramids coated with mercaptoundecanoic acid (red) and mercaptohexadecanoic acid (blue).

In summary, three strategies were employed in attempts to improve the sensitivity of nanoparticle film LSPR immunoassays. First, aptamers were used as capture molecules, bringing target proteins closer to the gold surface. Second, gold bipyramid substrates were fabricated, which have higher refractive index sensitivity and a narrower LSPR line width than gold nanorod substrates. This translates to an improved LSPR immunoassay sensitivity. Finally, improvement of sensitivity by decreasing the length of the SAM linking capture antibodies to the gold surface was demonstrated. Future detailed comparisons of different nanoparticles in LSPR immunoassays will require consideration of the chemical strategy for linking targeting agents such as antibodies to their surface.

V.   A Single Molecule Immunoassay by LSPR

Background

As shown in the previous chapters, LSPR can be the basis for sensing molecular interactions near the nanoparticle surface[86]. That is, one can directly measure molecular binding to a nanoparticle surface through minute changes in the particle's dielectric environment[87-89]. However, previous studies by us and others have not yet determined whether the LSPR mechanism can reach the ultimate sensing limit: the detection of individual molecules[90-92]. From a qualitative point of view, it is plausible that the scattering spectra from single plasmon resonant nanoparticles could transduce single-molecule events. Elongated gold and silver nanoparticles can have high refractive index sensitivities that are localized to nanometer-scale sensing volumes surrounding sharp tips[11, 12]. If a single macromolecule such as a protein with a refractive index different from water enters or leaves this sensing volume, one would expect a discernable shift in the peak wavelength of the plasmon resonance. Here we demonstrate single molecule LSPR detection by monitoring antibody-antigen unbinding events through the scattering spectra of individual gold bipyramids[66]. The unbinding rate is consistent with antibody-antigen binding kinetics determined from previous ensemble experiments[93, 94]. LSPR sensing could therefore be a powerful addition to the current toolbox of single molecule detection methods since it probes interactions on long timescales and under relatively natural conditions.

Methods

Atomic Force Microscopy (AFM) Characterization of Bipyramids. Bipyramids were deposited onto a glass cover slip by the previously described method of PEGylation and exposure to an APTES functionalized glass cover slip, followed by plasma cleaning[94]. AFM was carried out in tapping mode using a Veeco Nanoscope IV with a scan size of 4 microns and scan rate of 1 Hz.

Single particle optical measurements. Optical images and spectra were collected using a Zeiss Axiovert 200 microscope in an epi-illumination, dark-field scattering configuration, with an objective magnification of 50 X and numerical aperture of 0.5. In this geometry, incident light passes through an annular ring in the objective and is incident upon the sample at a high angle. Any light that is scattered back into the center of the objective by the sample is then routed to the detectors. A schematic of this setup appears in Figure 39.

50 X / NA 0.5

To CCD and spectrometer
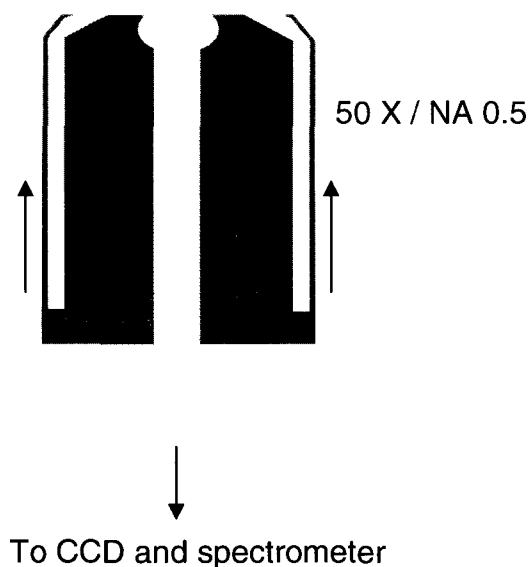
Figure 39. Schematic of the dark-field, epi-illumination microscopy setup used in single particle spectroscopy experiments.

Images were collected using a thermoelectrically cooled CCD camera (Roper PhotonMax). Single particle spectra were obtained by using a micromanipulation stage to align the particle with a slit located in a confocal imaging plane. The scattered light from the selected particle was analyzed using an Acton SpectraPro spectrograph and the aforementioned camera. Spectra were collected with integration times of 30-60 s.

In some cases, particles were located using alignment marks created by evaporating chrome and gold through an indexed TEM grid (Ted Pella, #79021C). Particles could be identified by their position relative to the alignment marks in both optical and scanning electron microscopy, making correlated measurements of the particle's spectrum and structure possible[95]. This technique is illustrated in Figure 40.
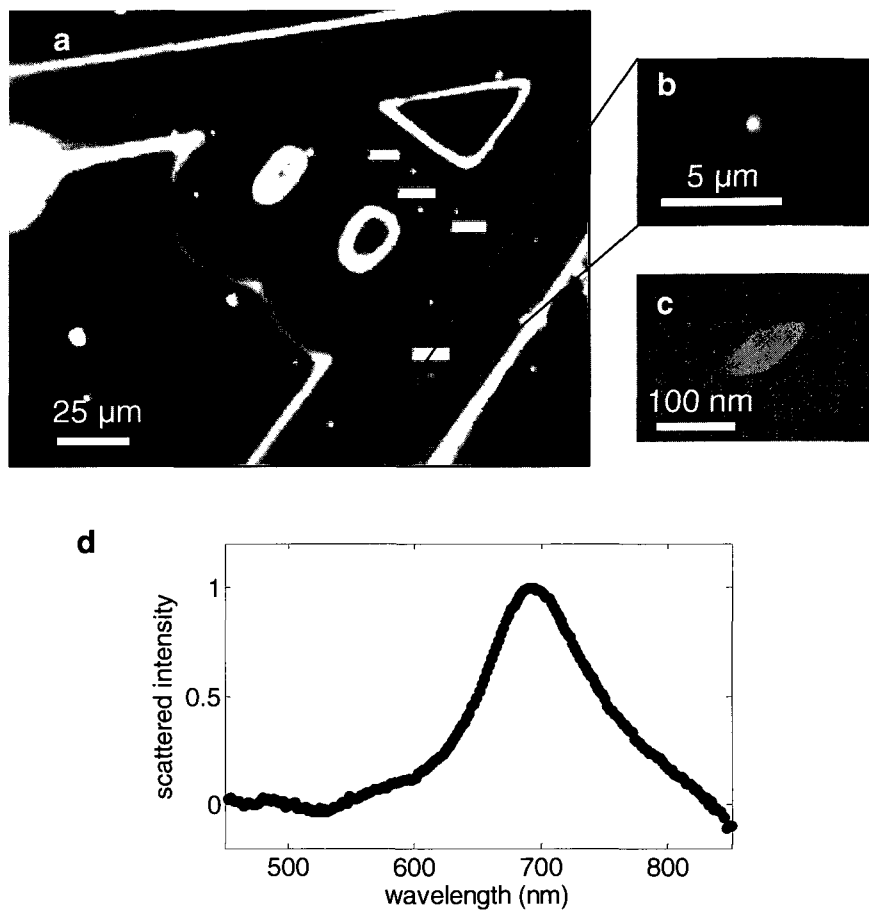
Figure 40. Single particle spectroscopy technique. (a) Alignment marks can be used to correlate images from (b) optical microscopy and (c) scanning electron microscopy. (d) shows the single particle spectrum of the bipyramid shown in (b) and (c).

Spectral analysis. Spectra were collected by the CCD camera in the form of spectrograph images of 512 x 512 pixels, in which the horizontal axis represents the particle's position in the slit, and the vertical axis represents wavelength. An example of the raw spectral data can be seen in Figure 41.
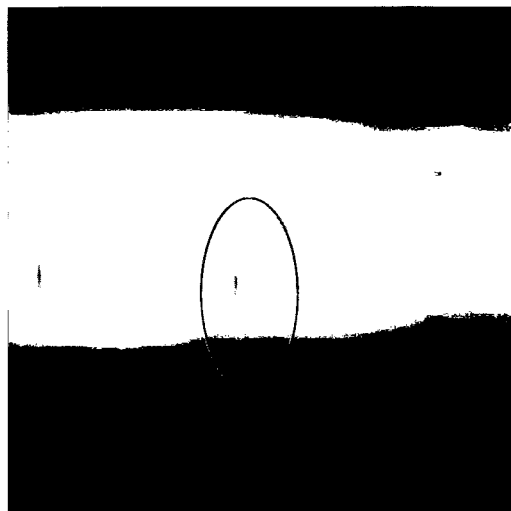
Figure 41. False-color image of raw spectral data from the single particle spectrometer, particle location circled in red.

The wavelength position on the CCD was calibrated using set of visible and near-infrared narrow bandpass filters (Chroma). To account for the variation of detector and spectrograph efficiency with wavelength, a white calibration was recorded from a reflection standard (Edmund Industrial Optics). The "whitecal" spectrum in raw counts can be seen in Figure 42. As one might expect for a microscope system optimized for the visible range, the peak detection sensitivity is between 500 and 700 nm.
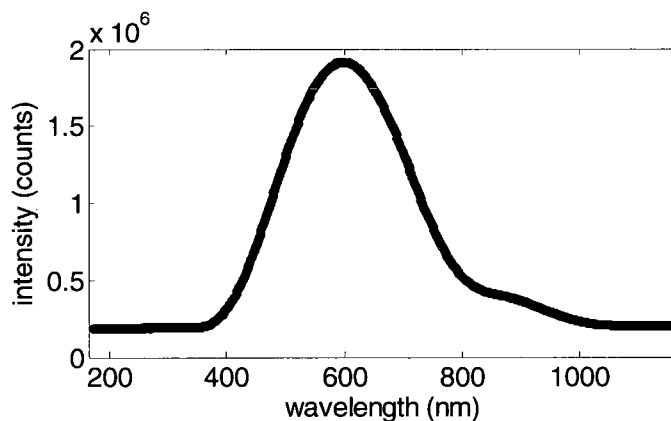
Figure 42. White-light calibration curve for the single-particle spectroscopy system. Experimental spectra are divided by this curve to account for the variation of detector sensitivity with wavelength.

A MATLAB program was developed to analyze the spectral images by summing the intensity at each wavelength within a few pixels of the particle, and subtracting the background intensity, then dividing by this whitecal. Each resulting spectrum was fit with a Gaussian, and the resulting peak wavelengths were plotted versus time.

Single particle immunoassay. To prepare a sparse film of particles, 40 μL of bipyramid solution was drop-cast onto a piranha-cleaned glass cover slip. (*WARNING*: piranha solution is very reactive and corrosive; use extreme caution!) The cover slip was then rinsed with copious amounts of DI water to remove CTAB. A flow cell was then assembled consisting of a 1 mm thick PDMS layer sandwiched between two layers of glass. The bottom glass layer (closest to the microscope objective) was the aforementioned cover slip with gold bipyramids deposited on the top side. The PDMS layer had a cut-out of approximately 2 x 10 mm in the center, creating a flow volume of about 20 μL. The top glass layer was a standard microscope slide, with two drilled holes sealed to syringe needles that served as the flow inlet and outlet. The entire assembly was placed on the microscope stage, and the particles were imaged through the bottommost cover slip. The flow system was regulated by a syringe pump on the outlet side of the flow cell, withdrawing liquid at a constant rate of 100 μL/min. Solutions entered from a set of reservoirs connected by a six-way valve to the flow cell. All components were connected with silicone tubing. The flow system was flushed through with buffer before each experiment to purge any air bubbles. In the immunoassay experiments, MES buffer (2-(N-morpholino)ethanesulfonic acid, 0.1 M) at pH 6.1 was first flowed over the substrate for at least 30 minutes. Next, the capture antibody, rabbit

IgG, was flowed over the substrate for at least 30 minutes at 300 μg/mL in MES buffer. Then, the substrate was rinsed with MES buffer for another 30 minutes to remove any excess capture antibody. Next, the target antibody, goat anti-rabbit IgG, was flowed over the substrate for at least 1 hour at 10 nM in PBS (phosphate buffered saline, 0.05 M with 0.15M NaCl) at pH 7.6. Finally, the substrate was rinsed for at least 8 hours in PBS.

Results and Discussion

Single gold bipyramids in the form of ten-sided polyhedra were chosen as the sensors for these experiments[66]. As synthesized here, they are approximately 140 nm long and 50 nm wide, and are monodisperse in terms of size and shape (Figure 43a). The bipyramids have sharp tips and are highly sensitive to the surrounding refractive index, with a figure of merit (FOM) greater than 4[84, 94]. Gold nanospheres are also present in the sample, but the bipyramids and nanospheres have distinct plasmon resonances as seen in their ensemble spectral extinction (Figure 43b). When the particles were deposited on a substrate and imaged by dark field microscopy, only the nanospheres were clearly visible to the eye since the bipyramid scattering is peaked at 875 nm. To illustrate how the particle types were differentiated, Figure 43d and e presents two dark-field optical images of a nanosphere (left) and a bipyramid (right), one taken by a color camera (d), where the nanosphere appears bright green and the bipyramid is extremely faint, and one taken by a near-infrared CCD (e), where the bipyramid appears much brighter. Scattering spectra of individual nanoparticles were recorded with an imaging spectrograph attached to the microscope. Figure 43c displays a single bipyramid's scattering spectrum collected with

a 30 second integration time. Note that the spectral peak is intense and relatively narrow, since the peak is in the near-infrared region where gold is minimally absorptive[14]. The peak near 520 nm in the ensemble extinction spectrum, attributable to the sphere impurities present in the sample, is no longer seen in the single particle scattering spectrum. It is also possible that the transverse plasmon resonance of the bipyramids contributes to the 520 nm peak in the ensemble spectrum, similar to the case for gold nanorods. If this mode were primarily absorptive rather than scattering, the single particle spectrum of Figure 43c would also result. FEM simulations (COMSOL) indicate that the transverse plasmon ought to contribute to the total extinction.
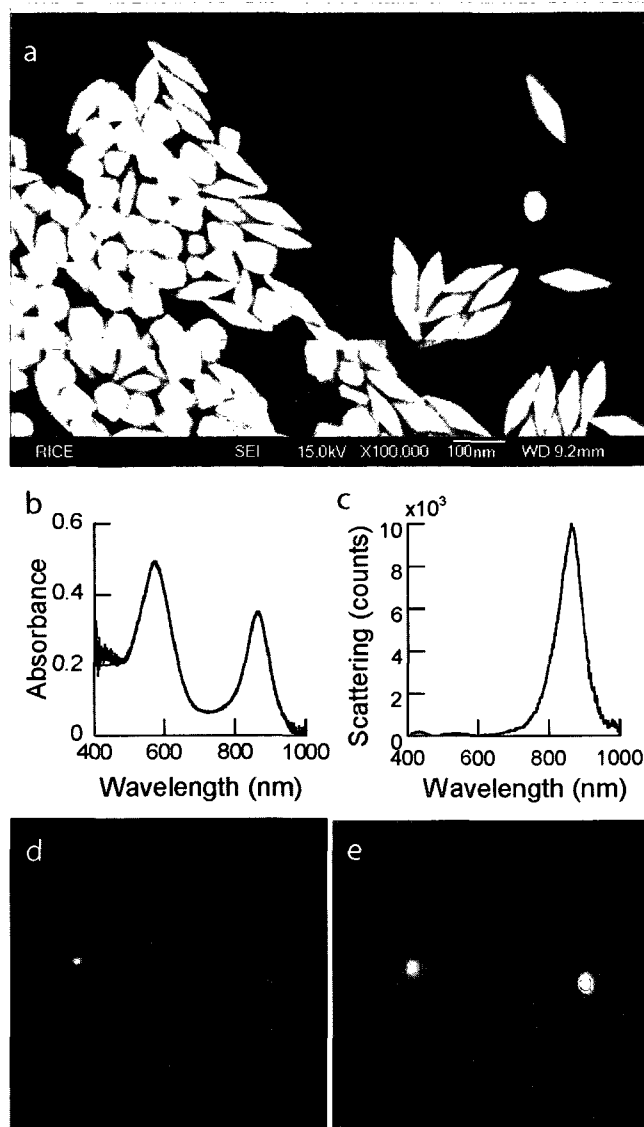
Figure 43. Gold bipyramids. (a) SEM image showing the bipyramids' structure. (b) Ensemble extinction measurement, showing the LSPR of nanospheres (580 nm) and bipyramids (875 nm). (c) Typical scattering spectrum of a single bipyramid. (d) Dark field scattering images of a nanosphere (left) and a bipyramid (right) captured with a colour camera and (e) captured with a CCD that is sensitive into the near-infrared.

In addition to the aforementioned favorable optical properties, the structure of the bipyramid and its orientation on the substrate enhance its sensing capabilities. Due to their faceted structure, bipyramids sit on the substrate with one tip elevated and exposed to the solution. This can be seen in the uneven contrast of the isolated bipyramids in

Figure 43a, and is shown more definitively by atomic force microscopy. Figure 44a displays the topography of the bipyramid sample with a 90 nm linear gray scale. The AFM images show uneven contrast in the topographic image of isolated bipyramids. Figure 44b displays the same image with a color scale designed to highlight variations in topography. Here one can see that one end of the isolated bipyramids slopes down while the other is flat. Finally, an AFM cross section is presented in Figure 44c and d that also supports the case that bipyramids sit on the substrate with one tip exposed to the solution. Because of this exposed sharp tip, the local refractive index of a molecular-scale volume in the solution can be monitored by tracking the LSPR peak of a single bipyramid. It is this extreme localization of the sensing volume, which is absent in nanoparticles of other shapes[13, 20, 24, 91, 92, 96-98], that makes bipyramids a strong candidate particle for single molecule detection.
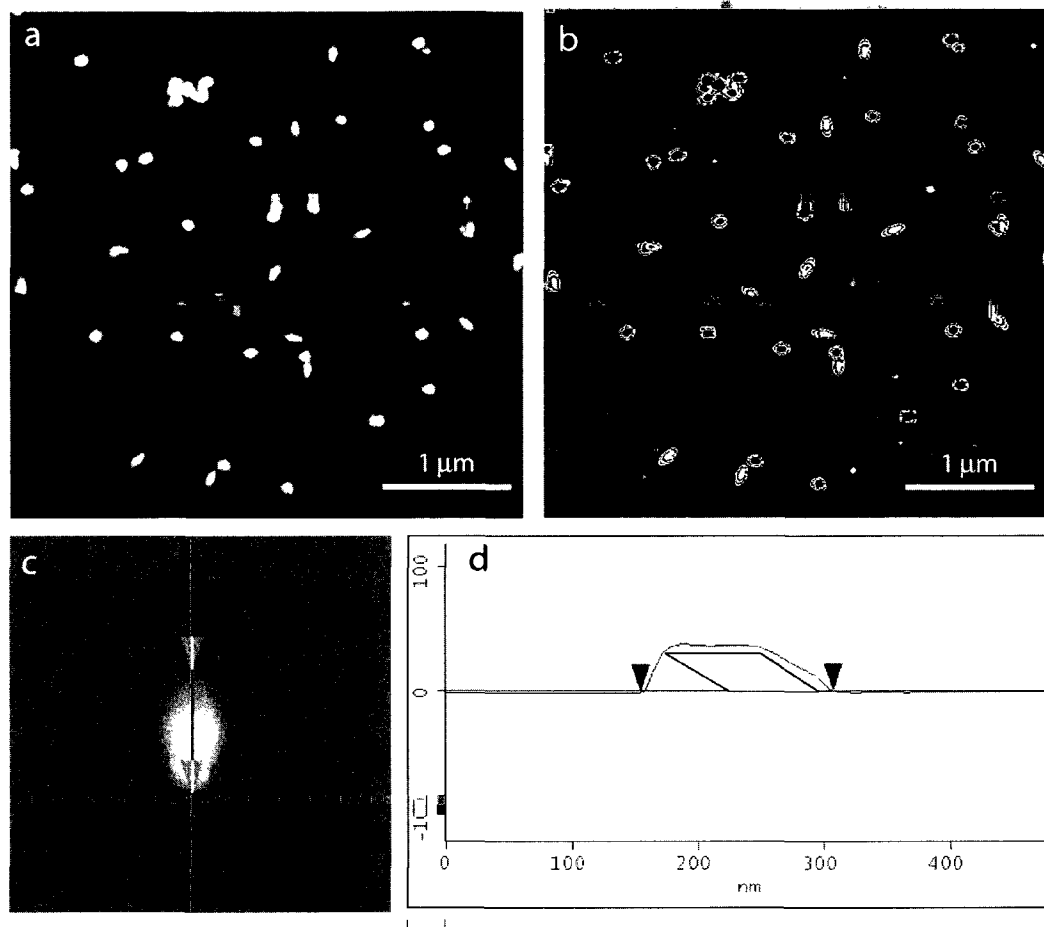
Figure 44. Bipyramid position on the substrate. (a) Atomic force microscopy of isolated gold bipyramids on a glass substrate with al linear gray scale. (b) The same image as in part a, but with a z-scale designed to highlight changes in height. (c) A zoom of one of the bipyramids in part a, with a line indicating a cross section. (d) The cross section drawn in part c which demonstrates the position of the bipyramids as indicated.

In the single-particle immunoassay experiments described here, bipyramid spectra were recorded over a period of 12 hours as the nanoparticle was exposed first to a capture antibody, then to a specific target molecule (a secondary antibody), and then rinsed with buffer (Figure 45).

Figure 45. Schematic of the single-particle immunoassay.

The LSPR peak wavelength shift versus time from a typical single-particle immunoassay experiment is shown in Figure 46a. At point 1, the capture antibody (rabbit IgG) was added and the spectrum red-shifted as antibodies coated the gold nanoparticle surface. At point 2 the target molecule (goat anti-rabbit IgG) was added and again the spectrum red-shifted, this time by a smaller amount since the target molecules are further from the bipyramid surface than the capture antibody. At point 3 the sample was rinsed once again. During this final rinse, single molecule events were detected as discrete blue-shifts in the LSPR peak wavelength due to the unbinding of single target molecules. We chose to study these single molecule unbinding events (as opposed to searching for discrete red shifts as molecules bind to the nanoparticle) because the dissociation is slow enough that one can measure the rate to confirm it matches an established value[93, 94]. In this case, the expected rate of dissociation of the target from the capture antibody is 6.5 x 10^{-5} s^{-1}, both from literature values and from our gold nanorod immunoassay described in the previous chapter, which used the same antibodies. Unlike the association rate, it should not be affected by the initial target concentration or any diffusion effects[93]. Thus, kinetics information can confirm that the observed events are indeed the antibody-antigen dissociation of interest.
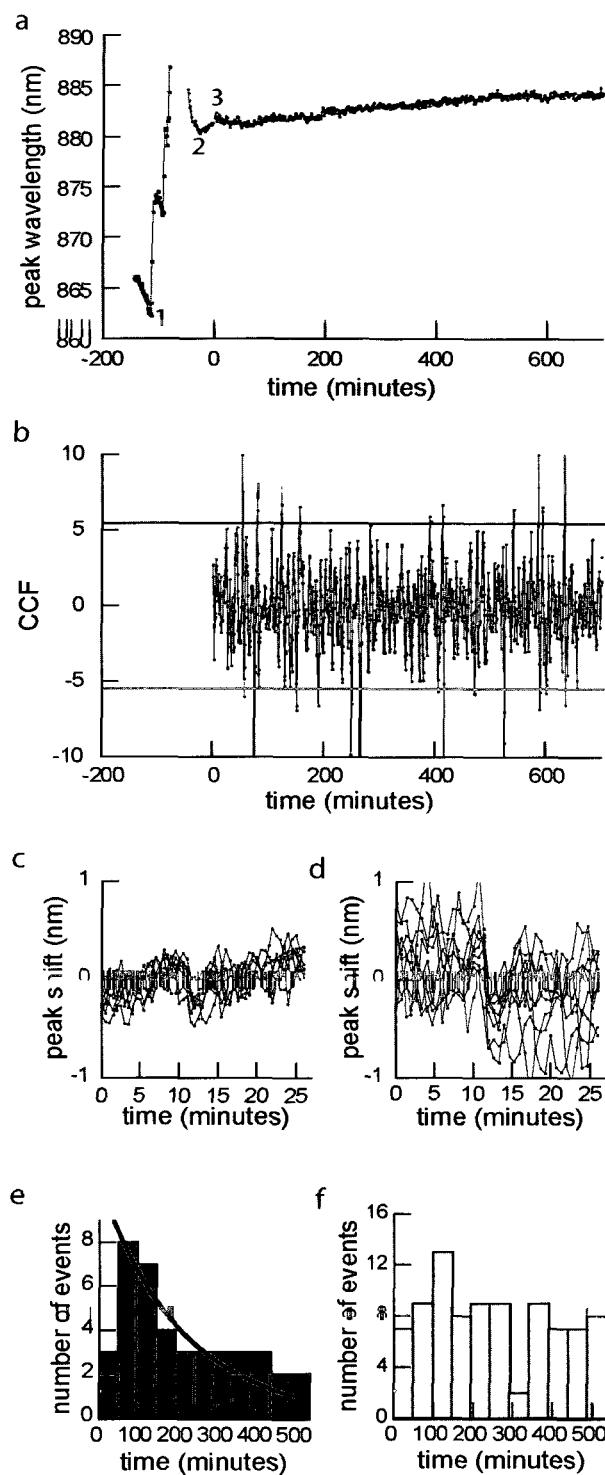
Figure 46. Single-particle immunoassay data. (a) LSPR signal obtained from single-particle spectra of a bipyramid in a flow cell, where it was exposed to (1) the capture antibody (Rabbit IgG), (2) the molecular target (Goat anti-Rabbit IgG), and (3) the PBS buffer rinse. (b) Cross-correlation function of the data with a step function. (c) and (d) Discrete blue shifts (i.e., single-molecule unbinding events) collected from two different experiments. (e) and (f), Histograms of all discrete blue and red shifts.

Both the measurements displayed in Figure 46 and the numerical simulations described below indicate that the LSPR peak shift due to single target molecule unbinding is only a few tenths of a nanometer, which is very close to the noise level (in this case the fluctuations in the measured LSPR peak wavelength). To analyze the data, we calculated the cross correlation function (CCF) between the measurements and a test function consisting of a discrete blue-shift at every point in the time series. For the sequence of six data points starting with the ith time step, the CCF was calculated as:

$$CCF = \frac{(\lambda_i + \lambda_{i+1} + \lambda_{i+2}) - (\lambda_{i+3} + \lambda_{i+4} + \lambda_{i+5})}{\sigma_1 + \sigma_2}$$ (32)

The numerator takes the form of the dot product of the data with a step function having the values (1, 1, 1, -1, -1, -1). This quantity is maximized when the data include a discrete blue shift between points ($i + 2$) and ($i + 3$), and minimized (i.e., CCF has a large negative value) when the data include a red shift. CCF is calculated for $i = 1$ through (N - 5), where N is the total length of the data series. In the denominator, σ_1 and σ_2 are the standard deviations in the data points i through ($i + 2$), and ($i + 3$) through ($i + 5$), respectively. Dividing by this factor enhances our ability to detect single molecule events because it will favor those events consisting of a clear step with low noise on either side. (This factor also accounts for the final cross-correlation having a magnitude greater than one in some cases, since this is not a standard normalization.) Once CCF has been calculated for the entire data series, the ten time points with the largest CCF values are designated as likely single molecule events.

The process is then repeated with one small difference: the cross-correlation is calculated for groupings of seven data points rather than six, in order to pick up those events which did not occur near the beginning of one of the 30 second CCD exposures.

As illustrated in Figure 47a, unbinding near the boundary between two exposures will produce the discrete shift described by the test function above. However, as illustrated in Figure 47b, unbinding near the middle of a frame will produce an intermediate peak wavelength since the frame will contain a sum of data from the blue and red peaks. For this case, the cross-correlation is calculated as:

$$CCF = \frac{(\lambda_i + \lambda_{i+1} + \lambda_{i+2}) - (\lambda_{i+4} + \lambda_{i+5} + \lambda_{i+6})}{\sigma_1 + \sigma_2}$$

(33)

where σ_1 and σ_2 are the standard deviations in the data points i through $(i + 2)$, and $(i + 4)$ through $(i + 6)$, respectively. The test function now has the values $(1, 1, 1, 0, -1, -1, -1)$. Again, the ten time points with the largest values of F are chosen.
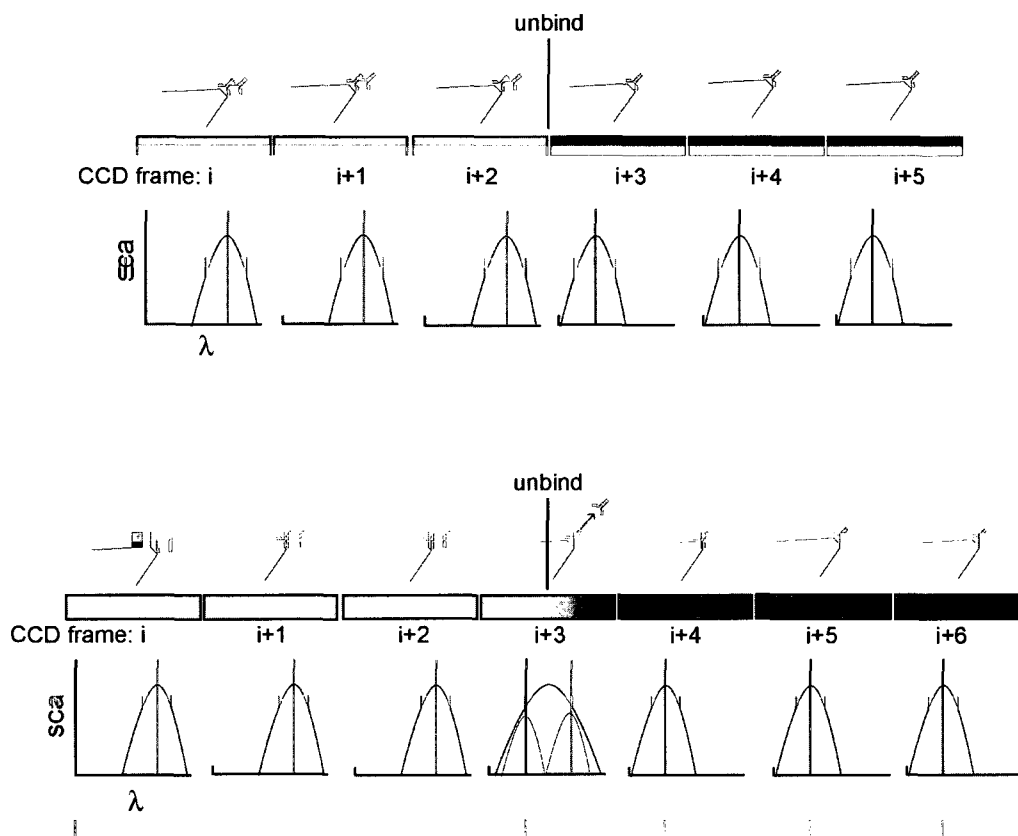
Figure 47. Schematic of unbinding event timing and detection. First row: When the molecule unbinds near the boundary of two frames, a discrete blue shift is measured between frames $(i + 2)$ and $(i + 3)$. Second row: When the molecule unbinds in the middle of an integration time, the spectral peak is artificially broadened in that frame, so a discrete shift can only be measured between frames $(i + 2)$ and $(i + 4)$.

Next, the ten likely single-molecule events from both cross-correlation functions are compared to check for redundancy. After deleting any duplicate events, the two lists are combined into one final group of times at which single-molecule dissociations occurred. The distribution of these times is then fit with an exponential probability density function to find τ, the lifetime of the antibody-antigen bond:

$$f(t) = \frac{1}{\tau} e^{-t/\tau} \qquad (34)$$

The unbinding rate is simply the inverse of the lifetime. Finally, the time data are sorted into a histogram (number of events vs. time) which can be seen in Figure 46e. The events with the lowest values of CCF (i.e., the largest red shifts) are collected in the same way, resulting in a histogram that reflects the random timing of these events.

The results of this analysis are plotted in Figures 46b-f. All of the blue-shifts from two experiments are plotted in Figure 46c and d. Note that the shift magnitude is greater for the experiment shown in (d), and that the data also has a higher noise level; this is due to slight variations in signal level and sensitivity among the individual bipyramids. The average blue-shift for all events was 0.34 nm. The probability distribution of single blue-shifts versus rinse time was fit with an exponential distribution and the unbinding rate was found to be 7.9 +/- 1.3 x 10^{-5} s^{-1}, in good agreement with ensemble measurements on the same antibody and molecular target[93, 94]. Finally, the time histograms of all blue-shift and red-shift events are plotted in Figure 46e and f. The histogram of red-shifts is featureless, indicating that these correspond to random fluctuations in the signal rather than a specific molecular process. The preponderance of discrete red-shifts is likely due to the gradual drift of the signal towards longer wavelengths upon the final rinse step (see Figure 46a).

To investigate the magnitude of LSPR shift that should be expected, finite element method (FEM) simulations were carried out with parameters that precisely matched the experimental conditions. (Note: this work was primarily carried out by Feng Hao of Peter Nordlander's research group.) A gold bipyramid (140 x 50 nm, 5 nm tip radius) was simulated to be sitting on a glass substrate ($n = 1.5$) in water ($n = 1.33$). Capture antibodies absorbed to the bipyramid were represented by a 5 nm dielectric film on the bipyramid. The film was assigned a refractive index of 1.57 to match previous determinations of the index of refraction of proteins[99]. The molecular target (secondary antibody) was simulated as a 7.1 nm diameter sphere, which was found by dividing its molecular weight by the average density of hydrated proteins[100]. The target was also given a dielectric constant of 1.57. Extinction spectra and maps of the local field intensity were calculated for the bipyramid both with and without the molecular target present at the tip. The field distribution around the bipyramid, displayed in Figure 48a-c, indicates the localization of the field enhancement around the tips. The calculated spectral extinction is comparable to the measured single bipyramid scattering spectra since the extinction for nanoparticles the size of these bipyramids is predominantly due to scattering. For the parameters given above, the spectral shift was found to be 0.45 nm, somewhat larger than our experimentally observed average shift of 0.34 nm. The protein dielectric constant was then varied and the simulations repeated. As seen in Figure 48d, the experimental shift is reproduced at $n = 1.54$, which suggests that this is the effective index of the individual antibody molecules.
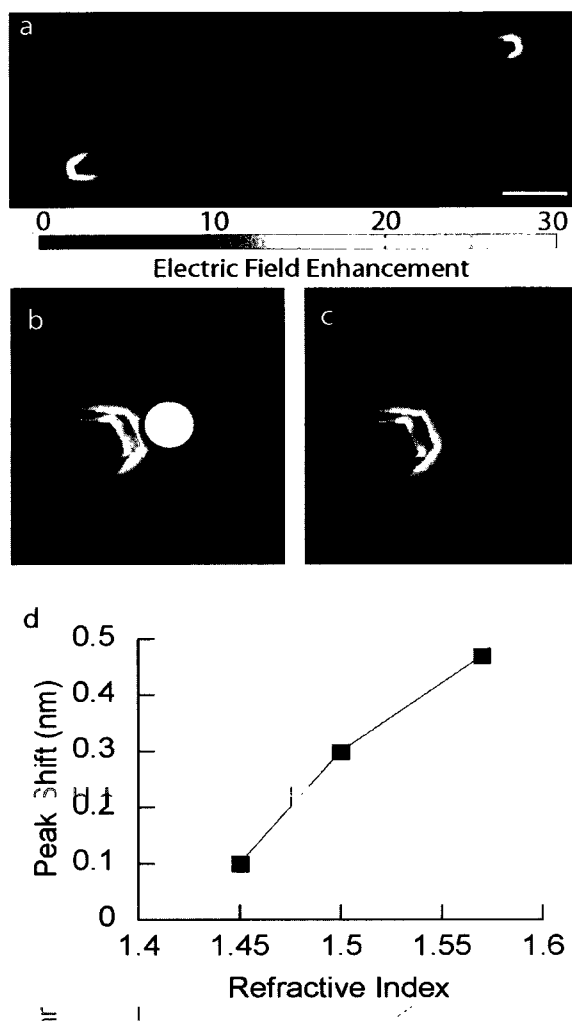
Figure 48. FEM simulations. (a) The electric field distribution around a gold bipyramid (scale bar is 20 nm). The local electric fields at the bipyramid tip (b) in the presence and (c) in the absence of a dielectric molecule. (d) The calculated spectral shift for molecules of differing refractive index.

The LSPR detection method described here has several unique properties that could address unmet needs in single molecule research. Foremost is the 10^5 second time scale over which LSPR sensing can observe molecular interactions. The most widespread single-molecule techniques are fluorescence-based methods such as fluorescence resonance energy transfer (FRET), in which researchers study conformation changes of macromolecules by introducing a distance-dependent pair of fluorophores[101]. This

technique has been combined with sensitive imaging methods like confocal fluorescence microscopy[102] and total internal reflectance fluorescence microscopy (TIRFM)[103] to investigate many biomolecular mechanisms. The main limitations of single-molecule fluorescence measurements are that (1) the molecules are removed from their natural state because of the fluorescent label and (2) due to photobleaching, the time scale for such experiments is limited to the order of 10^2 s. Another prominent class of single-molecule techniques depends on force sensing, either by optical tweezers or atomic force microscopy (AFM)[104]. These techniques allow us to study complex molecular motions, conformation changes, and energy landscapes. Of course, these techniques greatly perturb the molecules from their natural state, and in the case of optical tweezers, subject them to radiation damage from the laser. Stability challenges in force sensing experiments also limit the time duration of the experiments to the order of 10^2 seconds. Electrophysiological patch-clamp experiments on ion channels have also been carried out on single molecules[105]. These measurements are limited to a similar time scale due to the fragility of the membrane-pipette seal. Thus, the need for label-free, non-perturbative single molecule methods which can access longer time scales is clear.

Single molecule sensing by LSPR shifts also benefits from the non-invasive nature of the measurements. Since the target molecule's refractive index is detected, there is no need for chemical modification of the target or subsequent binding of other factors to it to generate a signal. Furthermore, the measurements are not taken under any applied load or tension, which are known to affect bond strengths in a load-rate dependent manner[106]. In single molecule LSPR experiments, the target molecule is only perturbed by the optical near-field of the nearby gold bipyramid[82].

The only other label-free, single molecule method previously reported was based on the effect of heat generated by optically irradiated biomolecules on a microtoroid resonator with a whispering gallery mode (WGM)[107]. (See Figure 49.) The WGM biosensor achieved a higher signal to noise ratio due to single molecule binding/unbinding, but this is not surprising since the WGM resonator exhibits a much higher quality factor than nanoparticle LSPR. However, the LSPR sensor has the advantage that it does not require microfabrication and can be monitored by simple far field optics. In fact, the bipyramid substrates described here were fabricated entirely by chemical synthesis and self assembly. This ultimate limit of detection achieved by WGM and now LSPR sensors could have significant impact in several biomedical areas including proteomics, point-of-care diagnostics, and drug discovery[86, 108].
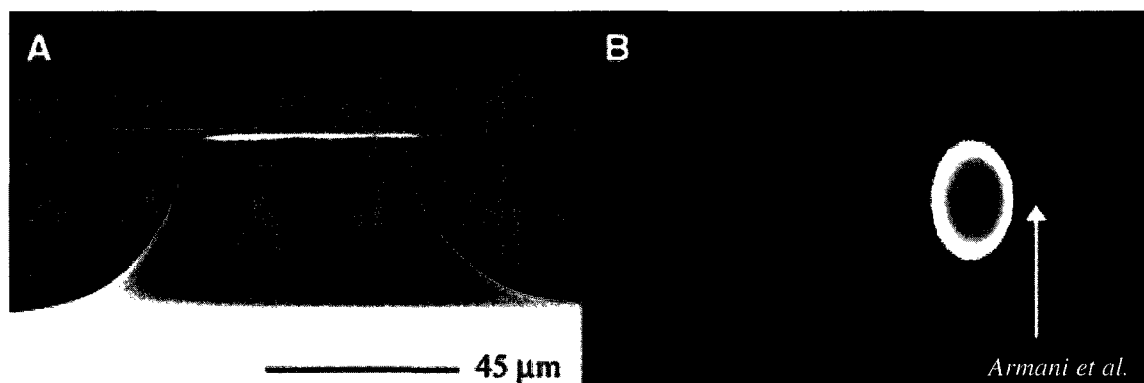
Figure 49. (a) The toroidal microresonator used for label-free single-molecule detection by Armani et al. (b) The optical whispering gallery mode (WGM) of the resonator.

In summary, due to their sharp tips, and bright, sharp spectral scattering resonances, gold bipyramids are well-suited for LSPR biosensing. The high sensitivity of the bipyramids allowed single-molecule antibody-antigen dissociation events to be observed with no labels and in real time. Analysis of the times at which these events occurred yielded an antibody-antigen unbinding rate of 7.9 +/- 1.3 x 10^{-5} s^{-1}, consistent with the

kinetic rate measured for an ensemble sample[93]. This is the first measurement of the

kinetics of a biomolecular bond by a label-free, single molecule method and shows that

LSPR sensing with simple optics and chemically synthesized nanoparticles holds great

promise as a biological sensing technology at the single molecule level.

VI.   Conclusion

Localized surface plasmon resonance provides a simple and robust system for refractive index sensing. The basis for this sensing is the extinction peak that arises from the resonant collective oscillation of the free electrons when excited by light. The electric field enhancement near the particle surface makes it possible to sensitively detect biomolecules in the small sensing volume surrounding the particle.   This was demonstrated for ensembles of nanoparticles with self-assembled gold nanorod films. A label-free immunoassay was designed based on this system, and specific antibody detection was demonstrated. The assay had nanomolar sensitivity, similar to SPR, and revealed the correct kinetic rates of association and dissociation and the correct equilibrium binding constant for antibody-antigen interactions.   This was the first demonstration of kinetics measurements by LSPR sensing.   Several routes to enhancement of the LSPR immunoassay sensitivity were investigated: the substrates were improved by replacing the gold nanorods with bipyramids, and by modifying the particle surface chemistry. Aptamers were also investigated as a capture molecule, as opposed to antibodies. A single molecule version of the immunoassay based on the scattering spectra of single gold bipyramids was also developed. By tracking discrete spectral shifts over long time periods, this technique was used to detect single molecules unbinding from the particle surface. Data analysis methods were developed to identify these events, and their measured magnitude agrees well with results from electrodynamic FEM simulations. These unbinding events were found to follow the time distribution

expected from the kinetics model. This was the first measurement of single molecules by

LSPR and is one of only a few label-free methods for studying single molecules.

VI.   References

1.   Mie, G., Articles on the optical characteristics of turbid tubes, especially colloidal metal solutions. Annalen Der Physik **1908**, 25, (3), 377-445.

2.   Bohren, C. F.; Huffman, D. R., Absorption and Scattering of Light by Small Particles. 2 ed.; Wiley-Interscience: 1998; p 544.

3.   Johnson, P. B.; Christy, R. W., Optical Constants of Noble Metals. Physical Review B **1972**, 6, (12), 4370-4379.

4.   Wagner, F. E.; Haslbeck, S.; Stievano, L.; Calogero, S.; Pankhurst, Q. A.; Martinek, P., Before striking gold in gold-ruby glass. Nature **2000**, 407, (6805), 691-692.

5.   Jensen, T. R.; Duval, M. L.; Kelly, K. L.; Lazarides, A. A.; Schatz, G. C.; Van Duyne, R. P., Nanosphere lithography: Effect of the external dielectric medium on the surface plasmon resonance spectrum of a periodic array of sliver nanoparticles. Journal of Physical Chemistry B **1999**, 103, (45), 9846-9853.

6.   Gans, R., The shape of ultra microscopic gold particles. Annalen Der Physik **1912**, 37, (5), 881-900.

7.   Eustis, S.; El-Sayed, M. A., Determination of the aspect ratio statistical distribution of gold nanorods in solution from a theoretical fit of the observed inhomogeneously broadened longitudinal plasmon resonance absorption spectrum. Journal of Applied Physics **2006**, 100, (4), -.

8.   Link, S.; El-Sayed, M. A., Correction: Simulation of the Optical Absorption Spectra of Gold Nanorods as a Function of Their Aspect Ratio and the Effect of the Medium Dielectric Constant. Journal of Physical Chemistry B **2005**, 109, (20), 10531-10532.

9.   Nehl, C. L.; Hafner, J. H., Shape-dependent plasmon resonances of gold nanoparticles. Journal of Materials Chemistry **2008**, 18, 2415-2419.

10.   Mock, J. J.; Barbic, M.; Smith, D. R.; Schultz, D. A.; Schultz, S., Shape effects in plasmon resonance of individual colloidal silver nanoparticles. Journal of Chemical Physics **2002**, 116, (15), 6755-6759.

11.   Nehl, C. L.; Liao, H. W.; Hafner, J. H., Optical properties of star-shaped gold nanoparticles. Nano Letters **2006**, 6, (4), 683-688.

12.   Hao, F.; Nehl, C. L.; Hafner, J. H.; Nordlander, P., Plasmon resonances of a gold nanostar. Nano Letters **2007**, 7, (3), 729-732.

13.   Sherry, L. J.; Chang, S.-H.; Schatz, G. C.; van Duyne, R. P., Localized Surface Plasmon Resonance Spectroscopy of Single Silver Nanocubes. Nano Letters **2005,** 5, (10), 2034-2038.

14.   Sönnichsen, C.; Franzl, T.; Wilk, T.; von Plessen, G.; Feldmann, J., Drastic Reduction of Plasmon Damping in Gold Nanorods. Physical Review Letters **2002,** 88, (7), 077402.

15.   Raschke, G.; Kowarik, S.; Franzl, T.; Sonnichsen, C.; Klar, T. A.; Feldmann, J.; Nichtl, A.; Kurzinger, K., Biomolecular recognition based on single gold nanoparticle light scattering. Nano Letters **2003,** 3, (7), 935-938.

16.   Tam, F.; Moran, C.; Halas, N., Geometrical parameters controlling sensitivity of nanoshell plasmon resonances to changes in dielectric environment. Journal of Physical Chemistry B **2004,** 108, (45), 17290-17294.

17.   Sun, Y.; Xia, Y., Increased Sensitivity of Surface Plasmon Resonance of Gold Nanoshells Compared to That of Gold Solid Colloids in Response to Environmental Changes. Analytical Chemistry **2002,** 74, 5297-5305.

18.   Wang, H.; Brandl, D. W.; Le, F.; Nordlander, P.; Halas, N. J., Nanorice: A hybrid plasmonic nanostructure. Nano Letters **2006,** 6, (4), 827-832.

19.   Underwood, S.; Mulvaney, P., Effect of the solution refractive index on the colors of gold colloids. Langmuir **1994,** 10, (10), 3427-3430.

20.   Raschke, G.; Brogl, S.; Susha, A. S.; Rogach, A. L.; Klar, T. A.; Feldmann, J.; Fieres, B.; Petkov, N.; Bein, T.; Nichtl, A.; Kurzinger, K., Gold nanoshells improve single nanoparticle molecular sensors. Nano Letters **2004,** 4, (10), 1853-1857.

21.   Malinsky, M. D.; Kelly, K. L.; Schatz, G. C.; Van Duyne, R. P., Nanosphere lithography: Effect of substrate on the localized surface plasmon resonance spectrum of silver nanoparticles. Journal of Physical Chemistry B **2001,** 105, (12), 2343-2350.

22.   Lee, J.; Hasan, W.; Odomt, T. W., Tuning the Thickness and Orientation of Single An Pyramids for Improved Refractive Index Sensitivities. Journal of Physical Chemistry C **2009,** 113, (6), 2205-2207.

23.   Mock, J. J.; Smith, D. R.; Schultz, S., Local refractive index dependence of plasmon resonance spectra from individual nanoparticles. Nano Letters **2003,** 3, (4), 485-491.

24.   Bukasov, R.; Shumaker-Parry, J. S., Highly Tunable Infrared Extinction Properties of Gold Nanocrescents. Nano Letters **2007,** 7, (5), 1113-1118.

25.   Malinsky, M. D.; Kelly, K. L.; Schatz, G. C.; Van Duyne, R. P., Chain length dependence and sensing capabilities of the localized surface plasmon resonance of silver

nanoparticles chemically modified with alkanethiol self-assembled monolayers. *Journal of the American Chemical Society* **2001**, *123*, *(7)*, 1471-1482.

26.   Haes, A. J.; Zou, S. L.; Schatz, G. C.; Van Duyne, R. P., Nanoscale optical biosensor: Short range distance dependence of the localized surface plasmon resonance of noble metal nanoparticles. *Journal of Physical Chemistry B* **2004**, *108*, *(22)*, 6961-6968.

27.   Elghanian, R.; Storhoff, J. J.; Mucic, R. C.; Letsinger, R. L.; Mirkin, C. A., Selective colorimetric detection of polynucleotides based on the distance-dependent optical properties of gold nanoparticles. *Science* **1997**, *277*, *(5329)*, 1078-1081.

28.   Harris, N. C.; Kiang, C. H., Defects can increase the melting temperature of DNA - Nanoparticle assemblies. *Journal of Physical Chemistry B* **2006**, *110*, *(33)*, 16393-16396.

29.   Englebienne, P., Use of colloidal gold surface plasmon resonance peak shift to infer affinity constants from the interactions between protein antigens and antibodies specific for single or multiple epitopes. *Analyst* **1998**, *123*, *(7)*, 1599-1603.

30.   Nath, N.; Chilkoti, A., A colorimetric gold nanoparticle sensor to interrogate biomolecular interactions in real time on a surface. *Analytical Chemistry* **2002**, *74*, *(3)*, 504-509.

31.   Haes, A. J.; Van Duyne, R. P., A nanoscale optical biosensor: Sensitivity and selectivity of an approach based on the localized surface plasmon resonance spectroscopy of triangular silver nanoparticles. *Journal of the American Chemical Society* **2002**, *124*, *(35)*, 10596-10604.

32.   Haes, A. J.; Van Duyne, R. P., Preliminary studies and potential applications of localized surface plasmon resonance spectroscopy in medical diagnostics. *Expert Review of Molecular Diagnostics* **2004**, *4*, *(4)*, 527-537.

33.   Wild, D., The Immunoassay Handbook. 3rd ed.; Elsevier: Amsterdam, The Netherlands, 2005.

34.   Karlsson, R., SPR for molecular interaction analysis: a review of emerging application areas. *Journal of Molecular Recognition* **2004**, *17*, *(3)*, 151-161.

35.   Ndieyira, J. W.; Watari, M.; Barrera, A. D.; Zhou, D.; Vogtli, M.; Batchelor, M.; Cooper, M. A.; Strunz, T.; Horton, M. A.; Abell, C.; Rayment, T.; Aeppli, G.; Mckendry, R. A., Nanomechanical detection of antibiotic mucopeptide binding in a model for superbug drug resistance. *Nature Nanotechnology* **2008**, *3*, *(11)*, 691-696.

36.   Chua, J. H.; Chee, R. E.; Agarwal, A.; Wong, S. M.; Zhang, G. J., Label-Free Electrical Detection of Cardiac Biomarker with Complementary Metal-Oxide Semiconductor-Compatible Silicon Nanowire Sensor Arrays. *Analytical Chemistry* **2009**, *81*, *(15)*, 6266-6271.

37.   Fagerstam, L. G.; Frostell, A.; Karlsson, R.; Kullman, M.; Larsson, A.; Malmqvist, M.; Butt, H., Detection of antigen-antibody interactions by surface plasmon resonance. Application to epitope mapping. Journal of Molecular Recognition *1990*, 3, 208-214.

38.   Safsten, P.; Klakamp, S.; Drake, A.; Karlsson, R.; Myszka, D., Screening antibody-antigen interactions in parallel using Biacore A100. ANALYTICAL BIOCHEMISTRY *2006*, 353, (2), 181-190.

39.   Cheng, S. F.; Chau, L. K., Colloidal gold-modified optical fiber for chemical and biochemical sensing. Analytical Chemistry *2003*, 75, (1), 16-21.

40.   Frederix, F.; Friedt, J. M.; Choi, K. H.; Laureyn, W.; Campitelli, A.; Mondelaers, D.; Maes, G.; Borghs, G., Biosensing based on light absorption of nanoscaled gold and silver particles. Analytical Chemistry *2003*, 75, (24), 6894-6900.

41.   Riboh, J. C.; Haes, A. J.; McFarland, A. D.; Yonzon, C. R.; Van Duyne, R. P., A nanoscale optical biosensor: Real-time immunoassay in physiological buffer enabled by improved nanoparticle adhesion. Journal of Physical Chemistry B *2003*, 107, (8), 1772-1780.

42.   Mitsui, K.; Handa, Y.; Kajikawa, K., Optical fiber affinity biosensor based on localized surface plasmon resonance. Applied Physics Letters *2004*, 85, (18), 4231-4233.

43.   Morokoshi, S.; Ohhori, K.; Mizukami, K.; Kitano, H., Sensing capabilities of colloidal gold modified with a self-assembled monolayer of a glucose-carrying polymer chain on a glass substrate. Langmuir *2004*, 20, (20), 8897-8902.

44.   Nath, N.; Chilkoti, A., Label-free biosensing by surface plasmon resonance of nanoparticles on glass: Optimization of nanoparticle size. Analytical Chemistry *2004*, 76, (18), 5370-5378.

45.   Yonzon, C. R.; Jeoungf, E.; Zou, S. L.; Schatz, G. C.; Mrksich, M.; Van Duyne, R. P., A comparative analysis of localized and propagating surface plasmon resonance sensors: The binding of concanavalin a to a monosaccharide functionalized self-assembled monolayer. Journal of the American Chemical Society *2004*, 126, (39), 12669-12676.

46.   Chen, H. H.; Suzuki, H.; Sato, O.; Gu, Z. Z., Biosensing capability of gold-nanoparticle-immobilized three-dimensionally ordered macroporous film. Applied Physics a-Materials Science & Processing *2005*, 81, (6), 1127-1130.

47.   Endo, T.; Yamamura, S.; Nagatani, N.; Morita, Y.; Takamura, Y.; Tamiya, E., Localized surface plasmon resonance based optical biosensor using surface modified nanoparticle layer for label-free monitoring of antigen-antibody reaction. Science and Technology of Advanced Materials *2005*, 6, (5), 491-500.

48.   Kalele, S. A.; Ashtaputre, S. S.; Hebalkar, N. Y.; Gosavi, S. W.; Deobagkar, D. N.; Deobagkar, D. D.; Kulkarni, S. K., Optical detection of antibody using silica-silver core-shell particles. Chemical Physics Letters **2005**, 404, (1-3), 136-141.

49.   Endo, T.; Kerman, K.; Nagatani, N.; Hiepa, H. M.; Kim, D. K.; Yonezawa, Y.; Nakano, K.; Tamiya, E., Multiple label-free detection of antigen-antibody reaction using localized surface plasmon resonance-based core-shell structured nanoparticle layer nanochip. Analytical Chemistry **2006**, 78, (18), 6465-6475.

50.   Fujiwara, K.; Watarai, H.; Itoh, H.; Nakahama, E.; Ogawa, N., Measurement of antibody binding to protein immobilized on gold nanoparticles by localized surface plasmon spectroscopy. Analytical and Bioanalytical Chemistry **2006**, 386, (3), 639-644.

51.   Kitano, H.; Anraku, Y.; Shinohara, H., Sensing capabilities of colloidal gold monolayer modified with a phenylboronic acid-carrying polymer brush. Biomacromolecules **2006**, 7, (4), 1065-1071.

52.   Kreuzer, M. P.; Quidant, R.; Badenes, G.; Marco, M. P., Quantitative detection of doping substances by a localised surface plasmon sensor. Biosensors & Bioelectronics **2006**, 21, (7), 1345-1349.

53.   Stewart, M. E.; Mack, N. H.; Malyarchuk, V.; Soares, J. A. N. T.; Lee, T. W.; Gray, S. K.; Nuzzo, R. G.; Rogers, J. A., Quantitative multispectral biosensing and 1D imaging using quasi-3D plasmonic crystals. Proceedings of the National Academy of Sciences of the United States of America **2006**, 103, (46), 17143-17148.

54.   Arai, T.; Kumar, P.; Rockstuhl, C.; Awazu, K.; Tominaga, J., An optical biosensor based on localized surface plasmon resonance of silver nanostructured films. JOURNAL OF OPTICS A-PURE AND APPLIED OPTICS **2007**, 9, (7), 699-703.

55.   Chen, C. D.; Cheng, S. F.; Chau, L. K.; Wang, C. R. C., Sensing capability of the localized surface plasmon resonance of gold nanorods. Biosensors & Bioelectronics **2007**, 22, (6), 926-932.

56.   Gish, D.; Nsiah, F.; McDermott, M.; Brett, M., Localized surface plasmon resonance biosensor using silver nanostructures fabricated by glancing angle deposition. ANALYTICAL CHEMISTRY **2007**, 79, (11), 4228-4232.

57.   Marinakos, S. M.; Chen, S. H.; Chilkoti, A., Plasmonic detection of a model analyte in serum by a gold nanorod sensor. Analytical Chemistry **2007**, 79, (14), 5278-5283.

58.   Miller, M. M.; Lazarides, A. A., Sensitivity of metal nanoparticle surface plasmon resonance to the dielectric environment. Journal of Physical Chemistry B **2005**, 109, (46), 21556-21565.

59.   Yu, C. X.; Irudayaraj, J., Multiplex biosensor using gold nanorods. Analytical Chemistry **2007**, 79, (2), 572-579.

60.   Haes, A. J.; Chang, L.; Klein, W. L.; Van Duyne, R. P., Detection of a biomarker for Alzheimer's disease from synthetic and clinical samples using a nanoscale optical biosensor. Journal of the American Chemical Society *2005*, 127, (7), 2264-2271.

61.   Haes, A. J.; Hall, W. P.; Chang, L.; Klein, W. L.; Van Duyne, R. P., A localized surface plasmon resonance biosensor: First steps toward an assay for Alzheimer's disease. Nano Letters *2004*, 4, (6), 1029-1034.

62.   Lin, T. J.; Huang, K. T.; Liu, C. Y., Determination of organophosphorous pesticides by a novel biosensor based on localized surface plasmon resonance. Biosensors & Bioelectronics *2006*, 22, (4), 513-518.

63.   Liao, H.; Hafner, J., Gold nanorod bioconjugates. Chemistry of Materials *2005*, 17, (18), 4636-4641.

64.   Sau, T. K.; Murphy, C. J., Room temperature, high-yield synthesis of multiple shapes of gold nanoparticles in aqueous solution. Journal of the American Chemical Society *2004*, 126, (28), 8648-8649.

65.   Nikoobakht, B.; El-Sayed, M. A., Preparation and growth mechanism of gold nanorods (NRs) using seed-mediated growth method. Chemistry of Materials *2003*, 15, (10), 1957-1962.

66.   Liu, M.; Guyot-Sionnest, P., Mechanism of Silver(I)-Assisted Growth of Gold Nanorods and Bipyramids. Journal of Physical Chemistry B *2005*, 109, (47), 22192-22200.

67.   Gulati, A.; Liao, H. W.; Hafner, J. H., Monitoring Gold Nanorod Synthesis by Localized Surface Plasmon Resonance. Journal of Physical Chemistry B *2006*, 110, 22323-22327.

68.   Liao, H. W.; Hafner, J. H., Monitoring gold nanorod synthesis on surfaces. Journal of Physical Chemistry B *2004*, 108, (50), 19276-19280.

69.   Hermanson, G. T., Bioconjugate Techniques. 1st ed.; Academic Press: 1996; p 785.

70.   Gao, J. X.; Bender, C. M.; Murphy, C. J., Dependence of the gold nanorod aspect ratio on the nature of the directing surfactant in aqueous solution. Langmuir *2003*, 19, (21), 9065-9070.

71.   Rostro, B. C.; Bickford, L.; Hafner, J. H., Stabilization and Targeting of Surfactant-Synthesized Gold Nanorods. Nanotechnology *2009*, In press.

72.   Lahiri, J.; Isaacs, L.; Tien, J.; Whitesides, G. M., A strategy for the generation of surfaces presenting ligands for studies of binding based on an active ester as a common reactive intermediate: A surface plasmon resonance study. Analytical Chemistry *1999*, 71, (4), 777-790.

73.   Love, J. C.; Estroff, L. A.; Kriebel, J. K.; Nuzzo, R. G.; Whitesides, G. M., Self-assembled monolayers of thiolates on metals as a form of nanotechnology. Chemical Reviews **2005**, 105, (4), 1103-1169.

74.   Hostetler, M. J.; Wingate, J. E.; Zhong, C. J.; Harris, J. E.; Vachet, R. W.; Clark, M. R.; Londono, J. D.; Green, S. J.; Stokes, J. J.; Wignall, G. D.; Glish, G. L.; Porter, M. D.; Evans, N. D.; Murray, R. W., Alkanethiolate gold cluster molecules with core diameters from 1.5 to 5.2 nm: Core and monolayer properties as a function of core size. Langmuir **1998**, 14, (1), 17-30.

75.   Liao, H.; Nehl, C. L.; Hafner, J. H., Biomedical applications of plasmon resonant metal nanoparticles. Nanomedicine **2006**, 1, (2), 201-208.

76.   Davies, C., Introduction to Immunoassay Principles. In The Immunoassay Handbook, 3 ed.; Wild, D., Ed. Elsevier: Amsterdam, The Netherlands, 2005; pp 3-40.

77.   Henzie, J.; Lee, M. H.; Odom, T. W., Multiscale patterning of plasmonic metamaterials. Nature Nanotechnology **2007**, 2, (9), 549-554.

78.   Nusz, G. J.; Curry, A. C.; Marinakos, S. M.; Wax, A.; Chilkoti, A., Rational Selection of Gold Nanorod Geometry for Labl-Free Plasmonic Biosenors. ACS Nano **2009**, 3, (4), 795-806.

79.   Bunka, D. H. J.; Stockley, P. G., Aptamers come of age - at last. Nature Reviews Microbiology **2006**, 4, (8), 588-596.

80.   Balamurugan, S.; Obubuafo, A.; Soper, S. A.; McCarley, R. L.; Spivak, D. A., Designing highly specific biosensing surfaces using aptamer monolayers on gold. Langmuir **2006**, 22, (14), 6446-6453.

81.   Balamurugan, S.; Obubuafo, A.; Soper, S. A.; Spivak, D. A., Surface immobilization methods for aptamer diagnostic applications. Analytical and Bioanalytical Chemistry **2008**, 390, (4), 1009-1021.

82.   Liu, M. Z.; Guyot-Sionnest, P.; Lee, T. W.; Gray, S. K., Optical properties of rodlike and bipyramidal gold nanoparticles from three-dimensional computations. Physical Review B **2007**, 76, (23), -.

83.   Murray, W. A.; Auguie, B.; Barnes, W. L., Sensitivity of Localized Surface Plasmon Resonances to Bulk and Local Changes in the Optical Environment. Journal of Physical Chemistry C **2009**, 113, (13), 5120-5125.

84.   Burgin, J.; Liu, M. Z.; Guyot-Sionnest, P., Dielectric Sensing with Deposited Gold Bipyramids. Journal of Physical Chemistry C **2008**, 112, (49), 19279-19282.

85.   Dong, Y. Z.; Shannon, C., Heterogeneous immunosensing using antigen and antibody monolayers on gold surfaces with electrochemical and scanning probe detection. Analytical Chemistry **2000**, 72, (11), 2371-2376.

86.   Anker, J. N.; Hall, W. P.; Lyandres, O.; Shah, N. C.; Zhao, J.; Van Duyne, R. P., Biosensing with plasmonic nanosensors. Nature Materials **2008**, 7, (6), 442-453.

87.   Stewart, M. E.; Anderton, C. R.; Thompson, L. B.; Maria, J.; Gray, S. K.; Rogers, J. A.; Nuzzo, R. G., Nanostructured plasmonic sensors. Chemical Reviews **2008**, 108, (2), 494-521.

88.   Willets, K. A.; Van Duyne, R. P., Localized surface plasmon resonance spectroscopy and sensing. Annual Review of Physical Chemistry **2007**, 58, 267-297.

89.   Hutter, E.; Fendler, J. H., Exploitation of localized surface plasmon resonance. Advanced Materials **2004**, 16, (19), 1685-1706.

90.   Haes, A. J.; Stuart, D. A.; Nie, S. M.; Van Duyne, R. P., Using solution-phase nanoparticles, surface-confined nanoparticle arrays and single nanoparticles as biological sensing platforms. Journal of Fluorescence **2004**, 14, (4), 355-367.

91.   Unger, A.; Rietzler, U.; Rudiger, B.; Kreiter, M., Sensitivity of Crescent-Shaped Metal Nanoparticles to Attachment of Dielectric Colloids. Nano Letters **2009**, ASAP.

92.   Larsson, E. M.; Alegret, J.; Kall, M.; Sutherland, D. S., Sensing characteristics of NIR localized surface plasmon resonances in gold nanorings for application as ultrasensitive biosensors. Nano Letters **2007**, 7, (5), 1256-1263.

93.   Mayer, K. M.; Lee, S.; Liao, H.; Rostro, B. C.; Fuentes, A.; Scully, P. T.; Nehl, C. L.; Hafner, J. H., A Label-Free Immunoassay based upon Localized Surface Plasmon Resonance of Gold Nanorods. ACS Nano **2008**, 2, 687-692.

94.   Lee, S.; Mayer, K. M.; Hafner, J. H., Improved Localized Surface Plasmon Resonance Immunoassay with Gold Bipyramid Substrates. Analytical Chemistry **2009**, 81, 4450-4455.

95.   Nehl, C.; Grady, N.; Goodrich, G.; Tam, F.; Halas, N.; Hafner, J., Scattering spectra of single gold nanoshells. Nano Letters **2004**, 4, (12), 2355-2359.

96.   Rindzevicius, T.; Alaverdyan, Y.; Dahlin, A.; Hook, F.; Sutherland, D. S.; Kall, M., Plasmonic sensing characteristics of single nanometric holes. Nano Letters **2005**, 5, (11), 2335-2339.

97.   Sherry, L. J.; Jin, R.; Mirkin, C. A.; Schatz, G. C.; Van Duyne, R. P., Localized Surface Plasmon Resonance Spectroscopy of Single Silver Triangular Nanoprisms. Nano Letters **2006**, 6, (9), 2060-2065.

98.   Baciu, C. L.; Becker, J.; Janshoff, A.; Sonnichsen, C., Protein-membrane interaction probed by single plasmonic nanoparticles. Nano Letters **2008**, 8, (6), 1724-1728.

99.   Jung, L. S.; Campbell, C. T.; Chinowsky, T. M.; Mar, M. N.; Yee, S. S., Quantitative interpretation of the response of surface plasmon resonance sensors to adsorbed films. Langmuir **1998**, 14, (19), 5636-5648.

100.   Squire, P. G.; Himmel, M. E., Hydrodynamics and Protein Hydration. Archives of Biochemistry and Biophysics **1979**, 196, (1), 165-177.

101.   Webb, S. E. D.; Roberts, S. K.; Needham, S. R.; Tynan, C. J.; Rolfe, D. J.; Winn, M. D.; Clarke, D. T.; Barraclough, R.; Martin-Fernandez, M. L., Single-molecule Imaging and fluorescence lifetime imaging microscopy show different structures for high- and low-affinity epidermal growth factor receptors in A431 cells. Biophysical Journal **2008**, 94, (3), 803-819.

102.   Shi, J.; Dertouzos, J.; Gafni, A.; Steel, D.; Palfey, B. A., Single-molecule kinetics reveals signatures of half-sites reactivity in dihydroorotate dehydrogenase A catalysis. Proceedings of the National Academy of Sciences of the United States of America **2006**, 103, (15), 5775-5780.

103.   Kuhn, J. R.; Pollard, T. D., Single molecule kinetic analysis of actin filament capping - Polyphosphoinositides do not dissociate capping proteins. Journal of Biological Chemistry **2007**, 282, (38), 28014-28024.

104.   Neuman, K. C.; Nagy, A., Single-molecule force spectroscopy: optical tweezers, magnetic tweezers and atomic force microscopy. Nature Methods **2008**, 5, (6), 491-505.

105.   Knight, A. E., Single molecule biology. Elsevier: Amsterdam, 2009; p 332.

106.   Merkel, R.; Nassoy, P.; Leung, A.; Ritchie, K.; Evans, E., Energy landscapes of receptor-ligand bonds explored with dynamic force spectroscopy. Nature **1999**, 397, (6714), 50-53.

107.   Armani, A. M.; Kulkarni, R. P.; Fraser, S. E.; Flagan, R. C.; Vahala, K. J., Label-free, single-molecule detection with optical microcavities. Science **2007**, 317, (5839), 783-787.

108.   Arnold, S.; Keng, D.; Shopova, S. I.; Holler, S.; Zurawsky, W.; Vollmer, F., Whispering gallery mode carousel - a photonic mechanism for enhanced nanoparticle detection in biosensing. Optics Express **2009**, 17, (8), 6230-6238.

VII.   Appendix 1: Additional Antibody-Antigen Kinetics Experiments
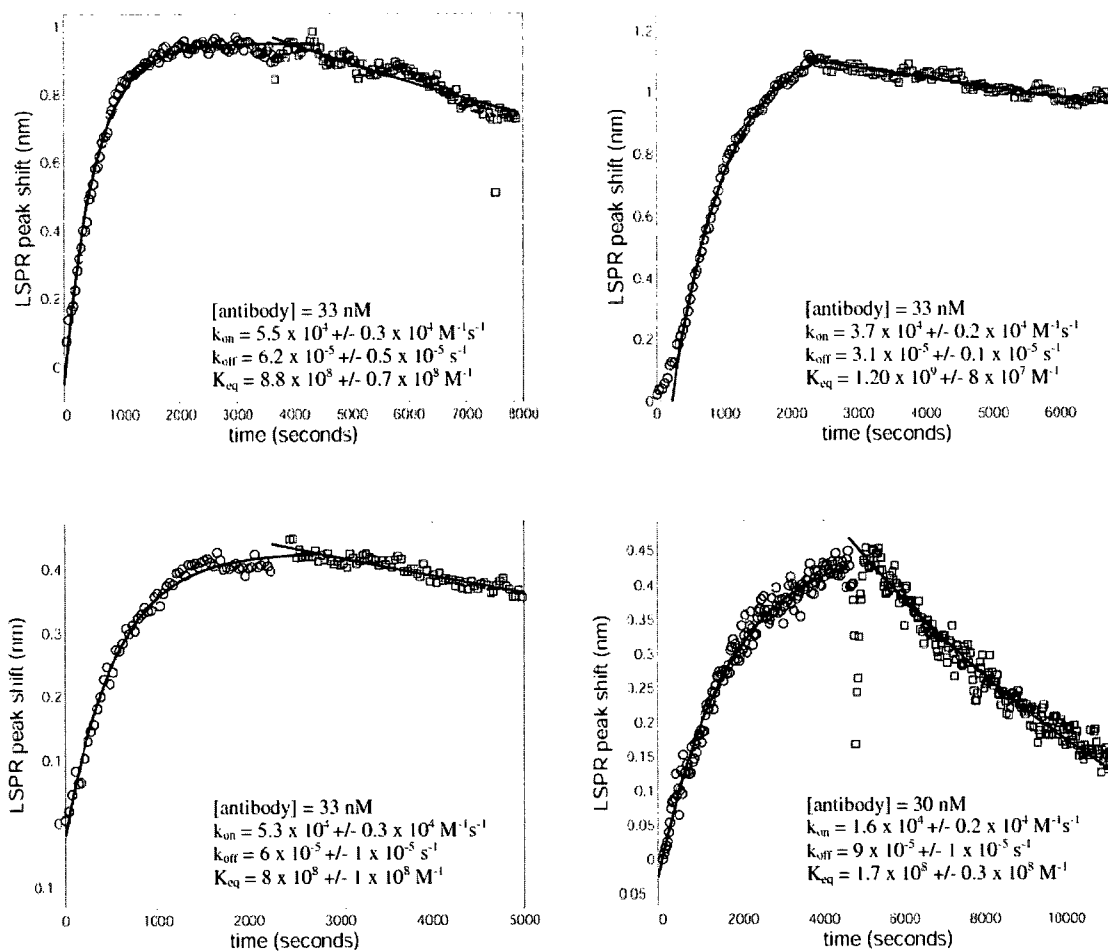

Figure 50. Four additional measurements of the kinetics of rabbit IgG / goat anti-rabbit IgG binding and unbinding as carried out by our LSPR system.

VIII. Appendix II: Detailed Bipyramid Film Spectra
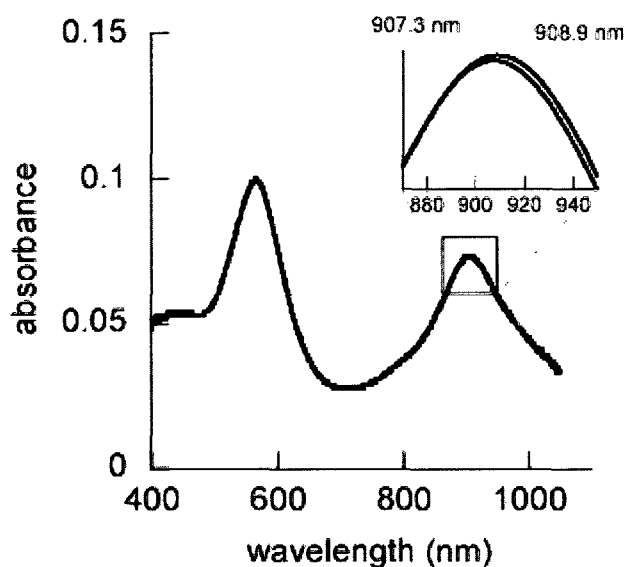

Figure 51. Endpoint spectra from the LSPR immunoassay. Spectra of the bipyramid film before and after the target antibody exposure (see Figure 5) are plotted on the main axis. The inset shows a magnified view of the fits to the peak.
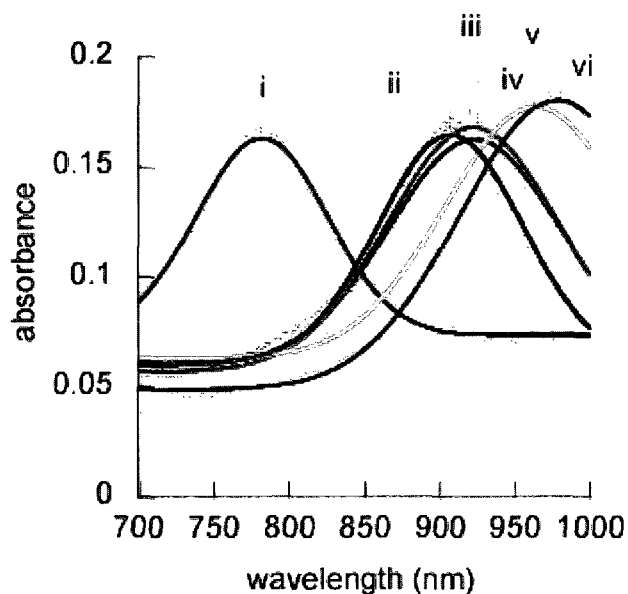

Figure 52. Spectra of bipyramid film IV (see Figure 4) in various solvents. In order of smallest to largest refractive index, the solvents are: air (i, red), water (ii, blue), acetonitrile (iii, pink), ethanol (iv, green), formamide (v, orange), and toluene (vi, purple).